

PatchEAD: Unifying Industrial Visual Prompting Frameworks for Patch-Exclusive Anomaly Detection

Po-Han Huang¹ Jeng-Lin Li¹ Po-Hsuan Huang¹ Ming-Ching Chang² Wei-Chao Chen¹
¹Inventec Corporation ²University at Albany, State University of New York

{huang.po-han, li.johncl, huang.reese, chen.wei-chao}@inventec.com mchang2@albany.edu

Abstract

Industrial anomaly detection is increasingly relying on foundation models, aiming for strong out-of-distribution generalization and rapid adaptation in real-world deployments. Notably, past studies have primarily focused on textual prompt tuning, leaving the intrinsic visual counterpart fragmented into processing steps specific to each foundation model. We aim to address this limitation by proposing a unified patch-focused framework, **Patch-Exclusive Anomaly Detection (PatchEAD)**, enabling training-free anomaly detection that is compatible with diverse foundation models. The framework constructs visual prompting techniques, including an alignment module and foreground masking. Our experiments show superior few-shot and batch zero-shot performance compared to prior work, despite the absence of textual features. Our study further examines how backbone structure and pretrained characteristics affect patch-similarity robustness, providing actionable guidance for selecting and configuring foundation models for real-world visual inspection. These results confirm that a well-unified patch-only framework can enable quick, calibration-light deployment without the need for carefully engineered textual prompts.

1. Introduction

Anomaly detection is a crucial area in computer vision that automates the identification of irregular regions in images, with applications for ensuring product quality and reducing costs in industrial settings. To avoid the need for collecting anomalous data, early research has increasingly focused on unsupervised, few-shot, or zero-shot learning methods. These approaches train models on a large number of normal samples, typically using either reconstruction-based [16, 18, 43, 44] or feature-based [2, 11, 34, 39] techniques. However, poor generalization to new domains or previously unseen anomalies remains a major challenge for real-world implementation.

Comparison of Patch-Only and Multi-Modality Methods

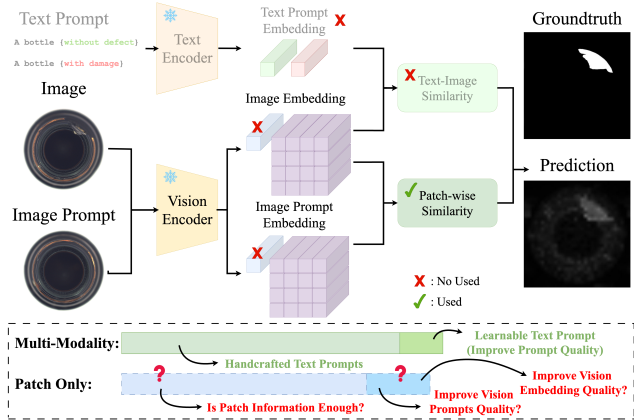


Figure 1. Comparison of patch-only (PatchEAD) and multi-modality industrial anomaly detection methods. We investigate whether a purely visual approach can achieve competitive performance of multi-modality methods, and whether further optimization of vision prompts can enhance effectiveness.

Foundation models pre-trained on large-scale datasets have recently demonstrated strong generalizability across domains and high accuracy on downstream tasks [27, 45]. Building on this, several works have leveraged such models for anomaly detection [7, 20, 32, 46, 47], pushing zero-shot and few-shot performance to new benchmarks. Despite this, the *one-model-fit-all* paradigm is not fully realized, as most approaches still rely heavily on additional module training and prompt tuning. The subsequent designs sometimes depend on the properties of the chosen foundation models. The complexity reduces adaptability in fast-evolving industrial environments [6], highlighting the need to unify a pipeline for foundation model deployments.

Intriguingly, we observe that previous studies mostly shape the pipeline using only textual prompt tuning, despite employing vision-language foundation models. A practical research question arises: *how can a unified pipeline be constructed using visual cues to support diverse modern foundation models?* In contrast to textual prompts expressing all

evidence through natural language, a pipeline with *patch-level visual prompts* requires a series of preprocessing and calibration designs for normal references. For example, the success of AnomalyDINO [10] is largely attributed to its tailored pipeline for DINOv2 [30], which was pretrained via self-supervised distillation for image representation learning. However, it remains unclear whether the same pipeline can be applied to CLIP or newer Perceptual Encoder (PE) models. The shortcoming of lacking a unified visual procedure parallels the challenge of highly varied textual prompting methods, limiting usability across scenarios. Therefore, we aim to identify a unified patch-only visual pipeline for training-free anomaly detection, as shown in Figure 6.

Following these observations, we introduce **Patch-Exclusive Anomaly Detection (PatchEAD)**, a framework based on patch-based feature comparison that excludes multi-modal features such as text and global image features. PatchEAD ensures high compatibility with any pretrained image-based model while maintaining anomaly detection performance. PatchEAD is designed for both batch zero-shot and few-shot settings (Figure 2), requiring no additional training, with a backbone-agnostic, vision-only patch-similarity formulation that standardizes usage across heterogeneous backbones and datasets. This design enhances industrial applicability and offers flexibility for future extension to different backbones.

We comprehensively evaluated PatchEAD on seven industrial anomaly datasets, comparing its performance with seven state-of-the-art (SoTA) few-shot [8, 11, 15, 20, 25, 34, 47] and four zero-shot or batch zero-shot [7, 20, 24, 46] anomaly detection methods. It achieves 96% image-level AUC on MVTec and 89.5% on VisA in the few-shot setting, and 95.3% on MVTec and 87.6% on VisA in the batch zero-shot setting. These results highlight its strong performance, on par with SoTA methods that require training or additional modalities.

Our contribution is summarized as follows:

- We investigate a practical foundation model problem in anomaly detection: the lack of unified visual-prompting pipeline. Our experiments address the generalization limitations of previous works that tailor visual processing to specific foundation models.
- We present the PatchEAD framework, characterized by its patch-only design, training-free nature, and compatibility with diverse foundation models. PatchEAD achieves SoTA anomaly detection results, underscoring the effectiveness of the unified visual pipeline even without relying on textual features.
- We further integrate alignment and background removal to create an enhanced version, PatchEAD⁺, which improves generalization and performance. This approach demonstrates the potential of a vision-centric augmentation strategy to strengthen patch-based frameworks.

2. Related Work

2.1. Unsupervised Anomaly Detection

The limited availability of abnormal samples often restricts current anomaly detection methods, making unsupervised learning approaches essential. One-class classification methods [23, 28, 37, 42] detect anomalies by modeling the distribution of normal samples and flagging outliers as anomalies. Reconstruction-based methods [16, 18, 43, 44] train autoencoders on large sets of normal samples, ensuring that abnormal samples are poorly reconstructed, thereby revealing anomaly regions. Knowledge distillation methods [14, 35] use discrepancies between teacher and student networks to identify anomalies. Memory bank methods [2, 11, 39] store features of normal images and detect anomalies by measuring feature distances. PatchCore [34] in particular demonstrates the effectiveness of local patch features, which outperform global image features in trained memory banks. Despite promising results, these methods often struggle to generalize across datasets, as they are constrained by training data size and feature extractor capacity.

2.2. Foundation Models in Anomaly Detection

Foundation models are widely used in recent anomaly detection methods due to their broad generalization capabilities. AnomalyCLIP [46] learns generalizable object-agnostic text prompts to adapt CLIP for distinguishing normal and abnormal cases. VCP-CLIP [32] uses visual context prompts to enhance CLIP’s ability to detect anomaly semantics, while PromptAD [25] appends abnormal suffixes to normal prompts and introduces an explicit anomaly margin for prompt learning. InCTRL [47] identifies anomalies by learning residuals between query images and normal prompts, improving cross-application generalization. AdaCLIP [7] incorporates learnable hybrid prompts for better adaptability in CLIP. These methods, however, often add significant computational overhead through prompt learning or additional model training.

Training-free approaches [12, 20] generally use hand-crafted text prompts, as in WinCLIP [20], which aligns multi-scale image features with a manually designed text prompt. Recently, MuSc [24] computes anomaly scores by comparing unlabeled test image patches, while AnomalyDINO [10] stores nominal patch representations from the reference samples in a memory bank and compares test patch features with these nominal representations.

Among these studies, only WinCLIP [20] explicitly evaluates applicability to both few-shot and zero-shot settings. Additionally, MuSc and AnomalyDINO adopt relatively complex multi-module designs, such as multi-scale aggregation or PCA-based mask extraction, which pose challenges for practical deployment. In contrast, our work emphasizes the differences in patch information, offering a

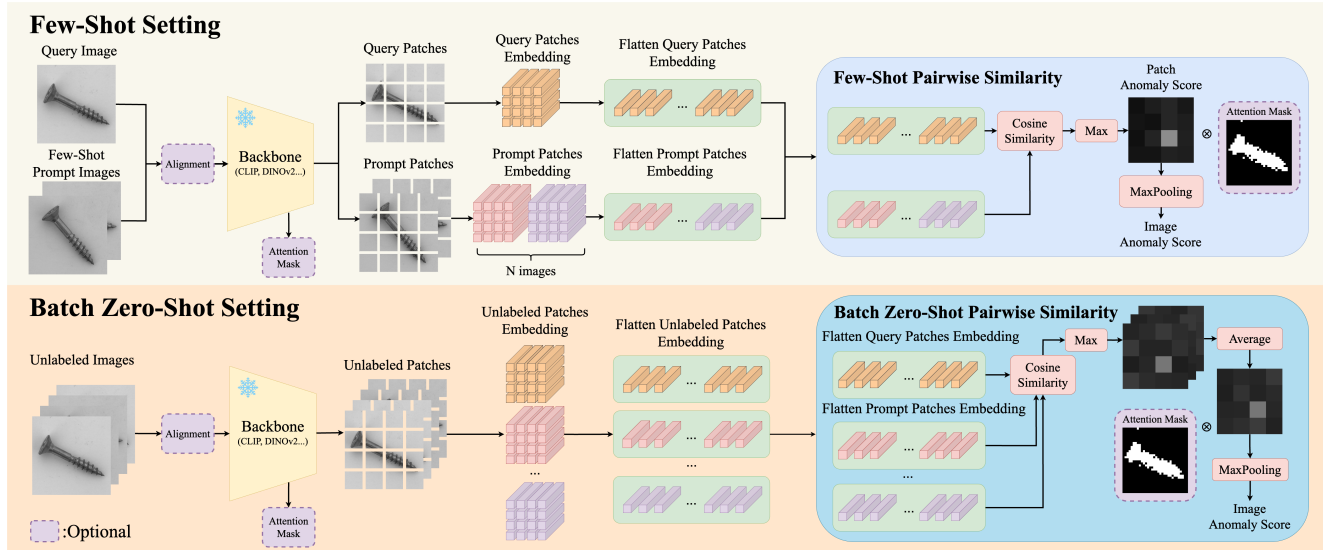


Figure 2. **The PatchEAD framework in few-shot and batch zero-shot settings:** In **few-shot**, normal prompt and query images are passed through the backbone to extract patch embeddings, which are flattened to compute patch-wise cosine similarities. The highest patch anomaly score is used as the image-level score. In **batch Zero-shot**, each image is compared to the rest of the batch using leave-one-out similarity, with its image-level anomaly score computed as the average of these scores. The version with optional alignment and masking modules is denoted as PatchEAD⁺.

comprehensive investigation of few-shot and batch zero-shot settings, demonstrating the effectiveness of a training-free, patch-only approach.

3. Method

Inspired by PatchCore [34], which shows that aggregating local patches preserves sufficient spatial information and avoids biases from the pretraining space, we first introduce our framework with few-shot and batch zero-shot settings in §3.1. §3.2 details the derivation of anomaly scores, and §3.3 presents techniques to improve the robustness of our patch-wise framework.

3.1. Patch-Exclusive Anomaly Detection

We emphasize the pivotal role of patch features and introduce the Patch-Exclusive Anomaly Detection (PatchEAD) framework (Figure 2). PatchEAD combines patch feature extraction with cross-patch scoring modules and supports both few-shot and batch zero-shot anomaly detection. By relying solely on patch-level information, it achieves robust, generalized performance.

Each whole image input $X \in \mathbb{R}^{W \times H}$, with width W and height H , is divided into equally sized, non-overlapping patches, forming a grid across the entire image. These patches are then individually processed by a frozen, pre-trained vision encoder $f_v(\cdot)$, which extracts feature embeddings for each patch. This method ensures that each patch independently represents a localized area of the image, capturing fine-grained spatial details while minimizing redun-

dancy across patches. This results in patch-level token embedding maps $E \in \mathbb{R}^{L \times D}$, where L denotes the number of patches and D is the embedding dimension, representing the visual characteristics of each patch.

We adopt a flexible choice of pre-trained vision encoder $f_v(\cdot)$ —including, but not limited to, models trained with self-supervised teacher-student objectives (e.g., DINOv2 [30]), cross-modality retrieval objectives (e.g., CLIP [33]), or any of the backbones evaluated in our ablation study. In each case, we retain only the visual branch—for example, dropping the [CLS] token in DINOv2 and removing the text encoder f_t in CLIP, ensuring that all patch features come purely from visual representations.

In the **few-shot** setting, we use N normal prompt images to establish anchors that enable the model to distinguish anomalies. In the **batch zero-shot** setting, framed here as an unsupervised anomaly-detection scenario, no precollected normal library is required; instead, we operate on a batch of unlabeled query images under the assumption that most samples in the test batch are normal. This differs from traditional methods that rely on a fixed pool of normal references. Specifically, following ACR [22] and MuSc [24], we treat each image in the batch as a query and use the remaining images as on-the-fly normal references to generate an anomaly prediction for that query. Repeating this process for every image yields a complete set of anomaly scores.

Table 1. **Comparisons of few-shot settings with state-of-the-art methods** on MVTec and VisA datasets. Scores are reported as $mean_{\pm std}$; training-based methods are shown in gray, and the highest score is highlighted in **bold red**.

Settings	Methods	Training Free	Patch Only	MVTec				VisA			
				Image-Level		Pixel-Level		Image-Level		Pixel-Level	
				AUC	AP	AUC	PRO	AUC	AP	AUC	PRO
1-shot	APIRL-GAN [8]			92.0 \pm 0.3	95.8 \pm 0.2	95.1 \pm 0.1	90.6 \pm 0.2	91.2 \pm 0.8	93.3 \pm 0.8	96.0 \pm 0.0	90.0 \pm 0.1
	AnomalyGPT [15]			94.1 \pm 1.1	-	95.3 \pm 0.1	-	87.4 \pm 0.8	-	96.2 \pm 0.1	-
	PromptAD [25]			94.6 \pm 1.7	-	95.9 \pm 0.5	-	86.9 \pm 2.3	-	96.7 \pm 0.4	-
	InCTRL [47]			-	-	-	-	-	-	-	-
	PaDiM [11]	✓	✓	76.6 \pm 3.1	88.1 \pm 1.7	89.3 \pm 0.9	73.3 \pm 2.0	62.8 \pm 5.4	68.3 \pm 4.0	89.9 \pm 0.8	64.3 \pm 2.4
	PatchCore [34]	✓	✓	83.4 \pm 3.0	92.2 \pm 1.5	92.0 \pm 1.0	79.7 \pm 2.0	79.9 \pm 2.9	82.8 \pm 2.3	95.4 \pm 0.6	80.5 \pm 2.5
	WinCLIP [20]	✓	✓	93.1 \pm 2.0	96.5\pm0.9	95.2 \pm 0.5	87.1 \pm 1.2	83.8 \pm 4.0	85.1 \pm 4.0	96.4 \pm 0.4	85.1 \pm 2.1
	PatchEAD (CLIP)	✓	✓	92.8 \pm 0.9	95.4 \pm 1.0	94.6 \pm 0.2	87.4 \pm 0.4	84.5 \pm 1.3	86.6 \pm 1.1	94.5 \pm 0.2	75.7 \pm 0.8
	PatchEAD+(CLIP)	✓	✓	93.4 \pm 0.8	96.2 \pm 0.6	94.9 \pm 0.2	88.0 \pm 0.5	86.2 \pm 0.6	87.7 \pm 0.9	95.6 \pm 0.1	79.8 \pm 0.1
	PatchEAD (DINOv2)	✓	✓	93.6 \pm 0.7	95.9 \pm 0.2	96.0 \pm 0.1	91.5 \pm 0.1	85.4 \pm 0.3	85.9 \pm 0.3	97.3 \pm 0.1	89.8 \pm 0.2
PatchEAD+(DINOv2)	✓	✓	95.0\pm0.6	97.0\pm0.2	96.1\pm0.2	91.6\pm0.1	89.1\pm0.4	89.7\pm0.5	97.4\pm0.1	90.6\pm0.2	
2-shot	APIRL-GAN [8]			92.4 \pm 0.3	96.0 \pm 0.2	95.5 \pm 0.0	91.3 \pm 0.1	92.2 \pm 0.3	94.2 \pm 0.3	96.2 \pm 0.0	90.1 \pm 0.1
	AnomalyGPT [15]			95.5 \pm 0.8	-	95.6 \pm 0.2	-	88.6 \pm 0.7	-	96.4 \pm 0.1	-
	PromptAD [25]			95.7 \pm 1.5	-	96.2 \pm 0.3	-	88.3 \pm 2.0	-	97.1 \pm 0.3	-
	InCTRL [47]			94.0 \pm 1.5	96.9 \pm 0.4	-	-	85.8 \pm 2.2	87.7 \pm 1.6	-	-
	PaDiM [11]	✓	✓	78.9 \pm 3.1	89.3 \pm 1.7	91.3 \pm 0.7	78.2 \pm 1.8	67.4 \pm 5.1	71.6 \pm 3.8	92.0 \pm 0.7	70.1 \pm 2.6
	PatchCore [34]	✓	✓	86.3 \pm 3.3	93.8 \pm 1.7	93.3 \pm 0.6	82.3 \pm 1.3	81.6 \pm 4.0	84.8 \pm 3.2	96.1 \pm 0.5	82.6 \pm 2.3
	WinCLIP [20]	✓	✓	94.4 \pm 1.3	97.0 \pm 0.7	96.0 \pm 0.3	88.4 \pm 0.9	84.6 \pm 2.4	85.8 \pm 2.7	96.8 \pm 0.3	86.2 \pm 1.4
	PatchEAD (CLIP)	✓	✓	92.8 \pm 0.5	95.5 \pm 0.4	94.8 \pm 0.1	87.6 \pm 0.3	87.8 \pm 1.4	89.4 \pm 1.7	95.6 \pm 0.1	78.8 \pm 0.2
	PatchEAD+(CLIP)	✓	✓	93.1 \pm 0.4	95.9 \pm 0.4	95.2 \pm 0.2	88.6 \pm 0.2	87.6 \pm 1.2	88.8 \pm 1.7	96.2 \pm 0.1	82.0 \pm 1.0
	PatchEAD (DINOv2)	✓	✓	95.0 \pm 0.1	96.6 \pm 0.3	96.3 \pm 0.1	92.1 \pm 0.1	87.7 \pm 0.3	88.0 \pm 0.5	97.7\pm0.1	90.8 \pm 0.2
PatchEAD+(DINOv2)	✓	✓	96.2\pm0.4	97.6\pm0.5	96.4\pm0.1	92.2\pm0.1	90.6\pm0.5	91.0\pm0.4	97.7\pm0.1	91.3\pm0.1	
4-shot	APIRL-GAN [8]			92.8 \pm 0.2	96.3 \pm 0.1	95.9 \pm 0.0	91.8 \pm 0.1	92.6 \pm 0.4	94.5 \pm 0.3	96.2 \pm 0.0	90.2 \pm 0.1
	AnomalyGPT [15]			96.3 \pm 0.3	-	96.2 \pm 0.1	-	90.6 \pm 0.7	-	96.7 \pm 0.1	-
	PromptAD [25]			96.6 \pm 0.9	-	96.5 \pm 0.2	-	89.1 \pm 1.7	-	97.4 \pm 0.3	-
	InCTRL [47]			94.5 \pm 1.8	97.2 \pm 0.6	-	-	87.7 \pm 1.9	90.2 \pm 2.7	-	-
	PaDiM [11]	✓	✓	80.4 \pm 2.5	90.5 \pm 1.6	92.6 \pm 0.7	81.3 \pm 1.9	72.8 \pm 2.9	75.6 \pm 2.2	93.2 \pm 0.5	72.6 \pm 1.9
	PatchCore [34]	✓	✓	88.8 \pm 2.6	94.5 \pm 1.5	94.3 \pm 0.5	84.3 \pm 1.6	85.3 \pm 2.1	87.5 \pm 2.1	96.8 \pm 0.3	84.9 \pm 1.4
	WinCLIP [20]	✓	✓	95.2 \pm 1.3	97.3 \pm 0.6	96.2 \pm 0.3	89.0 \pm 0.8	87.3 \pm 1.8	88.8 \pm 1.8	97.2 \pm 0.2	87.6 \pm 0.9
	PatchEAD (CLIP)	✓	✓	95.2 \pm 0.9	97.2 \pm 0.5	95.6 \pm 0.1	88.9 \pm 0.4	89.3 \pm 0.5	90.2 \pm 0.9	96.1 \pm 0.1	80.4 \pm 0.1
	PatchEAD+(CLIP)	✓	✓	95.2 \pm 0.8	97.2 \pm 0.5	95.9 \pm 0.1	89.6 \pm 0.3	89.5 \pm 0.3	90.5 \pm 0.3	96.7 \pm 0.1	82.8 \pm 0.5
	PatchEAD (DINOv2)	✓	✓	96.0 \pm 1.2	97.8 \pm 0.7	96.8 \pm 0.1	92.8 \pm 0.1	88.9 \pm 0.1	88.9 \pm 0.3	98.0\pm0.1	91.5 \pm 0.2
PatchEAD+(DINOv2)	✓	✓	97.0\pm0.8	98.3\pm0.4	96.9\pm0.1	92.9\pm0.2	91.9\pm0.3	92.3\pm0.6	98.0\pm0.1	92.1\pm0.1	

3.2. Cross-Patch Anomaly Scoring

We encode a query X_Q and N normal images $\{X_P\}_{i=1}^N$ into $\mathbf{E}_Q \in \mathbb{R}^{L \times D}$ and $\mathbf{E}_P \in \mathbb{R}^{N \times L \times D}$. The definition of the normal image set varies according to the targeted task. In the few-shot setting, a fixed number N of normal images is sampled. In contrast, the batch zero-shot setting considers a batch of B samples, treating each sample as a query and using the remaining $B - 1$ samples as normal references (*i.e.*, $N = B - 1$).

For a query patch j , the cosine distance to the k -th patch of the i -th normal image is

$$\mathbf{D}_{j,i,k} = 1 - \frac{\langle \mathbf{e}_Q^j, \mathbf{e}_P^{i,k} \rangle}{\|\mathbf{e}_Q^j\|_2 \|\mathbf{e}_P^{i,k}\|_2}, \quad (1)$$

A distance score for each normal image is represented by selecting the patch with the maximum distance in that image. Therefore, each query patch can obtain this distance

score relative to each image written as follows:

$$u_{j,i} = \max_{k \in \{1, \dots, L\}} \mathbf{D}_{j,i,k}, \quad (2)$$

Next, we aim to aggregate $u_{j,i}$ for the j^{th} patch as a patch-level anomaly score. The selected images are the top K_P highest-scoring images, denoted with the index set \mathcal{I}_P . The patch-level anomaly score for the j^{th} patch is the average score across these K images.

$$m_j = \frac{1}{K_P} \sum_{i \in \mathcal{I}_P} u_{j,i}. \quad (3)$$

We set $K_P = 1$ for the few-shot setting and $K_P = \max(1, 0.3N)$ for the batch zero-shot setting, *i.e.*, the top 30% of images are used to compute patch-level anomaly scores. Each patch thus obtains the score based on the normal images that exhibit the most significant deviations.

Table 2. Comparisons of batch zero-shot *image-level* (top) and *pixel-level* (bottom) performance with state-of-the-art methods across multiple datasets. Training-based methods are shown in gray, and the highest score is highlighted in bold red. Base versions of all networks are used for fair comparison at similar model sizes. † indicates methods reproduced using official code and weights.

Image-level evaluation	Training Free	Patch Only	MVTec[3]		VisA[48]		MPDD[21]		BTAD[29]		KSDD[38]		DAGM[41]		DTD-Syn.[1]		Average	
			AUC	AP														
AnomalyCLIP [46]			91.5	96.2	82.1	85.4	77.0	82.0	88.3	87.3	84.7	80.0	97.5	92.3	93.5	97.0	87.8	88.6
AdaCLIP† [7]			89.9	95.7	86.1	88.2	69.5	74.6	90.4	94.1	96.9	91.1	96.9	88.2	91.5	95.4	88.7	89.6
WinCLIP [20]	✓		91.8	96.5	78.1	81.2	63.6	69.9	68.2	70.9	84.3	77.4	91.8	79.5	93.2	92.6	81.6	81.1
MuSc† [24]	✓		95.8	98.2	88.1	90.1	68.6	74.1	95.4	98.9	92.6	67.6	95.2	85.8	90.6	95.8	89.5	87.2
PatchEAD (CLIP)	✓	✓	94.5	97.0	86.8	88.0	69.5	75.5	92.3	96.8	89.0	63.5	92.5	78.7	92.4	97.2	88.1	85.2
PatchEAD+ (CLIP)	✓	✓	94.6	97.1	86.9	88.9	70.6	75.9	91.5	95.3	89.4	66.3	94.3	80.4	91.9	96.4	88.5	85.8
PatchEAD (DINOv2)	✓	✓	94.3	97.0	87.5	87.3	65.3	70.3	92.3	96.0	93.7	67.2	97.6	89.7	91.4	96.0	88.9	86.2
PatchEAD+ (DINOv2)	✓	✓	95.9	97.9	92.2	92.6	68.6	71.8	91.2	94.3	97.0	85.5	98.3	92.8	97.6	98.8	91.5	90.5

Pixel-level evaluation	Training Free	Patch Only	MVTec[3]		VisA[48]		MPDD[21]		BTAD[29]		KSDD[38]		DAGM[41]		DTD-Syn.[1]		Average	
			AUC	PRO														
AnomalyCLIP [46]			91.1	81.4	95.4	87.0	96.5	88.7	94.2	74.8	90.6	67.8	95.6	91.0	97.9	92.3	94.5	83.3
AdaCLIP† [7]			89.9	44.1	95.8	53.5	92.9	30.1	93.7	20.3	95.9	33.6	92.4	36.1	96.9	68.1	93.9	40.8
WinCLIP [20]	✓		85.1	64.6	79.6	56.8	76.4	48.9	72.7	27.3	68.8	24.2	87.6	65.7	83.9	57.8	79.2	49.3
MuSc† [24]	✓		97.2	91.8	97.5	82.1	96.9	90.7	97.9	77.5	96.4	82.2	96.8	93.6	97.6	93.9	97.2	87.4
PatchEAD (CLIP)	✓	✓	95.0	88.9	96.5	79.1	94.0	82.7	96.4	71.2	97.6	86.4	94.9	88.0	97.9	92.0	96.0	84.0
PatchEAD+ (CLIP)	✓	✓	94.4	87.9	96.3	79.3	94.3	84.8	96.5	72.3	97.7	87.1	95.3	89.4	97.7	91.2	96.0	84.6
PatchEAD (DINOv2)	✓	✓	95.9	91.3	96.9	87.5	95.9	89.3	97.4	78.7	99.2	94.8	97.2	94.2	97.9	92.6	97.2	89.8
PatchEAD+ (DINOv2)	✓	✓	95.6	91.4	97.7	91.2	96.6	89.6	97.0	80.0	99.3	97.7	96.4	92.6	98.3	95.1	97.3	91.1

Finally, the query image can derive an image-level score by averaging over its top K_I patch scores:

$$S = \frac{1}{K_I} \sum_{j \in \mathcal{I}_I} m_j, \quad (4)$$

where $K_I = \max(1, \rho L)$, and \mathcal{I}_I is the corresponding top- K_I index set. This anomaly score S determines the final prediction of the image.

3.3. PatchEAD+: Visual Prompt Enhancement

We integrated optional alignment and masking features as part of the visual prompting techniques to enhance object alignment across images and reduce false positives from object edges and background noise. We refer to this *visual prompt-enhanced* version as PatchEAD+ in the following experiments. Alignment reduces patch drift, and masking reduces background interference. Additional implementation details are provided in the supplementary material.

Alignment: Object misalignment can cause patches to shift or rotate, resulting in higher anomaly scores during patch matching, especially at object edges. To address this, we use a feature-matching method from traditional image processing to align images through rotation and translation, ensuring consistent positioning and orientation between prompt and query images.

Masking: We normalize the model’s final-layer attention scores to the $[0, 1]$ range and apply a predefined threshold to binarize the result, producing a foreground mask that suppresses background regions. This approach mitigates the risk of misclassification caused by background noise.

4. Experimental Evaluation

Datasets: We conducted extensive evaluation experiments on **seven** widely used industrial anomaly detection datasets to assess the performance of our PatchEAD framework: MVTec [3], VisA [48], MPDD [21], BTAD [29], KSDD [38], DAGM [41], and DTD-Synthetic [1]. These datasets collectively include over 50 different classes and defect types, providing a comprehensive testbed for real-world applications. PatchEAD was compared with **five** state-of-the-art (SoTA) methods for few-shot anomaly detection: AprilGAN [8], AnomalyGPT [46], PromptAD [25], InCTRL [47], and WinCLIP [20], as well as **four** leading zero-shot/batch zero-shot methods: AnomalyCLIP [46], AdaCLIP [46], WinCLIP [20], and MuSc [24]. These comprehensive comparisons demonstrate the training-free applicability of our framework across diverse datasets and detection settings.

Evaluation Metrics: For a comprehensive comparison with previous methods, we followed [46] in using the Area Under the Receiver Operating Characteristic Curve (AUC) as an evaluation metric at both image and pixel levels. Additionally, we include image-level Average Precision (AP) and pixel-level Per-Region Overlap (PRO) [4] to better assess the model’s performance on imbalanced datasets and its ability to localize anomalous regions.

4.1. Implementation Details

Model architecture: For the reproduced CLIP-based model, we utilized the pre-trained ViT-B/16+ from OpenCLIP [19], following the WinCLIP, MuSc, and AdaCLIP approaches to ensure a fair comparison. We also exper-

imented with DINOv2 [30] and chose the ViT-B/14 distilled(with registers) variants as the backbone.

Few-shot setting: We randomly sampled N images from the training set of each category as prompts, where $N \in \{1, 2, 4\}$. To ensure robust results, we used three random seeds for sampling and reported the mean and standard deviation across trials.

Batch Zero-shot setting: We evaluated batch zero-shot anomaly detection using batches of 64 unlabeled queries and processed most data in a single pass without replication. This setup is consistent with the approach used in ACR [22] and MuSc [24].

4.2. Details of Alignment and Masking

We introduce both alignment and masking to the MVTec, VisA, KSDD, DAGM, and DTD-Synthetic datasets, and only masking is applied to MPDD and BTAD due to the objects being well-aligned (BTAD) or undergoing 3D rotation (MPDD).

Alignment: In the few-shot setting, we calculate the displacement and rotation between each prompt image and the query image. We then add the corrected images and their 180-degree rotations to the prompt list to ensure consistent positions and angles during patch matching. In the zero-shot setting, we use the first image as the query and apply the same process to all other images. For similarity calculation, we average the scores from the three images for each sample to determine the final anomaly score.

Masking: We extract the final attention layer and average all attention heads to get the [CLS] token’s attention scores for each patch. Given that the values vary substantially across model architectures and images, we first min-max normalize the attention scores to 0, 1. After normalizing, patches with scores above 0.05 are set to 1, and those below to 0.5. This reduces the incorrect activations in background areas.

4.3. Few-/Batch Zero-Shot Detection Results

Our experimental results cover both few-shot and batch zero-shot settings, aligning closely with prior works. Table 1 presents the **few-shot** results where the methods requiring training are shown in grey. While these training-based methods offer an upper bound on performance, they are often impractical for real-world use. Our proposed PatchEAD⁺ (DINOv2) achieves remarkable performance in both image-level and pixel-level detection, approaching this upper bound.

PatchEAD (CLIP) achieves performance comparable to WinCLIP across different datasets and N-shot settings, demonstrating that patch-level information alone can deliver competitive results. Furthermore, using a more vision-centric backbone such as DINOv2, along with techniques like feature alignment and background removal to enhance

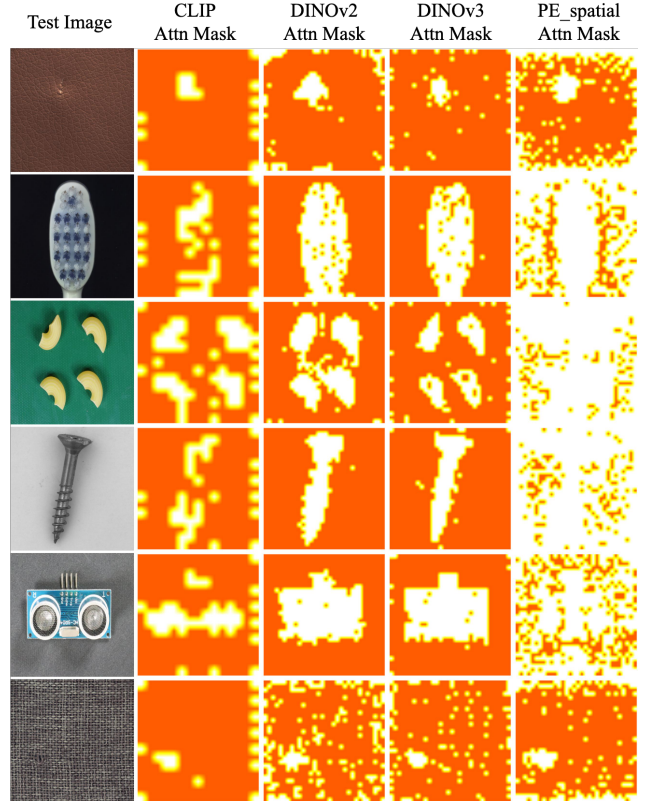


Figure 3. Visualization of attention masks from different backbones across normal and abnormal images, demonstrating the ability to down-weight noisy regions.

the quality of visual prompts, further improves performance. These results demonstrate that, for anomaly detection tasks, both factors can provide benefits similar to those achieved with textual prompts.

The **batch zero-shot** results in Table 2 show that our PatchEAD models outperform WinCLIP. PatchEAD⁺ (DINOv2) achieves an average image-level AUC of 91.5% and AP of 90.5% across seven datasets, surpassing WinCLIP by 9.4% in AUC and 9.9% in AP. These results also outperform those of MuSc under the same batch zero-shot setting, even with MuSc’s advanced rescoring modules that leverage multi-level patch granularity. This demonstrates that higher-quality vision embeddings and enhanced vision prompts can significantly improve the cross-patch similarity framework.

4.4. Attention Mask Visualization

We visualize the attention between the CLS token and patch tokens using four foundation models: CLIP, DINOv2, DINOv3, and PE_spatial, as shown in Figure 3. Under the aforementioned masking rules, we observe that DINOv2 and DINOv3 exhibit the strongest capability in capturing foreground regions, while CLIP tends to focus on a

Table 3. **Ablation study on backbone selection**, evaluating alternative architectures: MAE [17], BEiTv2 [31], EVA-02 [13], PE_spatial [5], and DINOv3 [36], to assess their performance impact on image-level AUC (I-AUC) and pixel-level AUC (P-AUC) for MVTec and VisA datasets.

Setup	PatchEAD backbone	MVTec [3]		VisA [48]	
		I-AUC	P-AUC	I-AUC	P-AUC
Batch 0-shot	MAE [17]	85.2	94.3	64.2	80.6
	BEiTv2 [31]	84.9	91.6	74.2	88.7
	EVA-02 [13]	91.75	91.3	85.8	92.9
	DINOv2 [30]	94.3	95.9	87.5	96.9
	PE_spatial [5]	95.1	96.7	90.6	97.8
	DINOv3 [36]	95.6	97.5	88.1	97.0
1-shot	MAE [17]	77.6±0.4	90.7±0.1	56.7±2.5	76.5±0.3
	BEiTv2 [31]	86.8±1.0	91.4±0.4	75.9±0.2	86.7±0.1
	EVA-02 [13]	90.6±1.6	91.5±0.3	80.5±0.6	91.6±0.1
	CLIP [33]	91.6±0.7	94.5±0.3	81.6±0.9	94.5±0.2
	DINOv2 [30]	93.6±0.7	96.0±0.1	85.4±0.3	97.3±0.1
	PE_spatial [5]	93.1±0.3	96.3±0.2	88.0±0.7	96.8±0.1
2-shot	MAE [17]	79.5±0.5	91.8±0.4	59.1±0.7	78.2±0.3
	BEiTv2 [31]	87.7±0.5	91.9±0.2	77.3±0.9	87.8±0.3
	EVA-02 [13]	92.7±0.6	91.8±0.1	87.2±0.4	92.5±0.1
	CLIP [33]	91.6±0.6	94.8±0.1	85.3±1.1	95.6±0.1
	DINOv2 [30]	95.0±0.1	96.3±0.1	87.7±0.3	97.7±0.1
	PE_spatial [5]	93.1±0.5	96.5±0.2	90.6±0.4	97.3±0.1
4-shot	MAE [17]	82.7±0.4	93.5±0.1	66.0±1.1	80.4±0.3
	BEiTv2 [31]	89.1±0.3	92.6±0.1	78.5±0.3	88.8±0.2
	EVA-02 [13]	94.1±1.1	92.5±0.1	90.0±0.5	93.0±0.1
	CLIP [33]	94.1±0.8	95.6±0.1	86.7±0.3	96.1±0.1
	DINOv2 [30]	96.0±1.2	96.8±0.1	88.9±0.1	98.0±0.1
	PE_spatial [5]	95.1±0.7	97.0±0.1	92.8±0.1	97.6±0.1
4-shot	DINOv3 [36]	94.4±0.6	96.8±0.1	89.4±0.5	96.2±0.2

Table 4. **Ablation study** on the impact of image size using DINOv2, highlighting effects on patch receptive fields. I-AUC and P-AUC denote image- and pixel-level AUC, respectively. 0-shot indicates the batch zero-shot setting.

Setting	Image Size	MVTec [3]		VisA [48]	
		I-AUC	P-AUC	I-AUC	P-AUC
0-shot	224x224	90.7	93.6	82.8	93.2
0-shot	448x448	94.3	95.9	87.5	96.9
0-shot	672x672	94.7	96.4	89.1	97.5
4-shot	224x224	94.7±0.8	94.4±0.1	85.1±0.2	92.7±0.1
4-shot	448x448	96.0±1.2	96.8±0.1	88.9±0.1	98.0±0.1
4-shot	672x672	96.2±0.8	96.7±0.1	91.2±0.4	97.3±0.1

few localized areas, and PE_spatial produces comparatively smoother attention distributions. Nevertheless, all models consistently assign relatively high attention scores to defect regions. In our strategy, attention values below the threshold are down-weighted rather than set to zero, which improves the generalizability of the approach.

4.5. Ablation Study

Comparison of model architecture: We use MAE [17], BEiTv2 [31], EVA-02 [13], PE_spatial [5], and DI-

Table 5. **Ablation study** on the impact of different modules in PatchEAD⁺ (DINOv2), highlighting the contribution of each component. I-AUC and P-AUC denote image- and pixel-level AUC, respectively. 0-shot refers to the batch zero-shot setting.

Setting	Module		MVTec [3]		VisA [48]	
	Alignment	Attn Mask	I-AUC	P-AUC	I-AUC	P-AUC
0-shot			94.3	95.9	87.5	96.9
0-shot	✓		94.8	95.0	85.7	96.4
0-shot		✓	95.6	96.2	91.8	97.9
0-shot	✓	✓	95.9	95.6	92.2	97.7
4-shot			96.0±1.2	96.8±0.1	88.9±0.1	98.0±0.1
4-shot	✓		97.0±0.8	96.1±0.1	90.1±0.1	96.7±0.1
4-shot		✓	96.4±0.8	96.9±0.1	91.8±0.3	97.9±0.1
4-shot	✓	✓	97.0±0.8	96.9±0.1	91.9±0.3	98.0±0.1

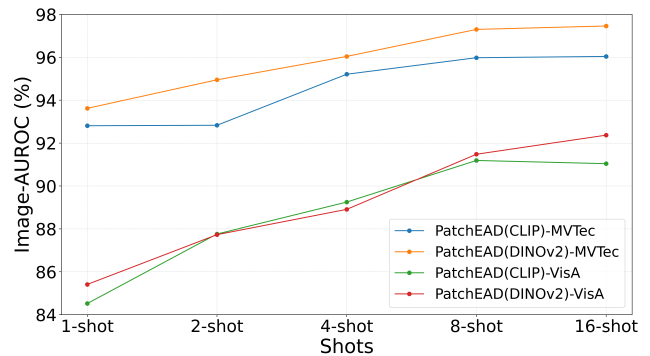


Figure 4. **Ablation study** on the effect of the number of few-shot images in PatchEAD on image-level AUC for MVTec and VisA datasets.

NOv3 [36] as our backbone models to analyze the impact of model size and architecture. As shown in Table 3, once the backbone reaches moderate capacity, this training-free, pure patch-similarity scheme produces consistently strong results in MVTec and VisA and different settings, highlighting the robust generalization of the framework.

Increasing number of few-shot normal images: We investigated the impact of increasing the number of shots to determine whether patch information could be further enhanced with more reference images. As shown in Figure 4, varying the number of inferencing shots from 1 to 16 led to a clear upward trend in image-level AUC scores. The most significant improvements were observed with 1-8 shots, with diminishing returns beyond that. Notably, increasing the number of shots beyond 16 yielded only marginal additional benefits. This experiment highlights a practical trade-off, emphasizing the need to balance few-shot data collection with adaptation efficiency.

Effects of increasing image size: We investigated the impact of varying input image size on anomaly detection performance, which is a crucial factor influencing the model’s receptive field, as our implementation maintains a constant patch size. Experiments on the MVTec [3] and VisA [48] datasets are shown in Table 4. The results revealed consis-

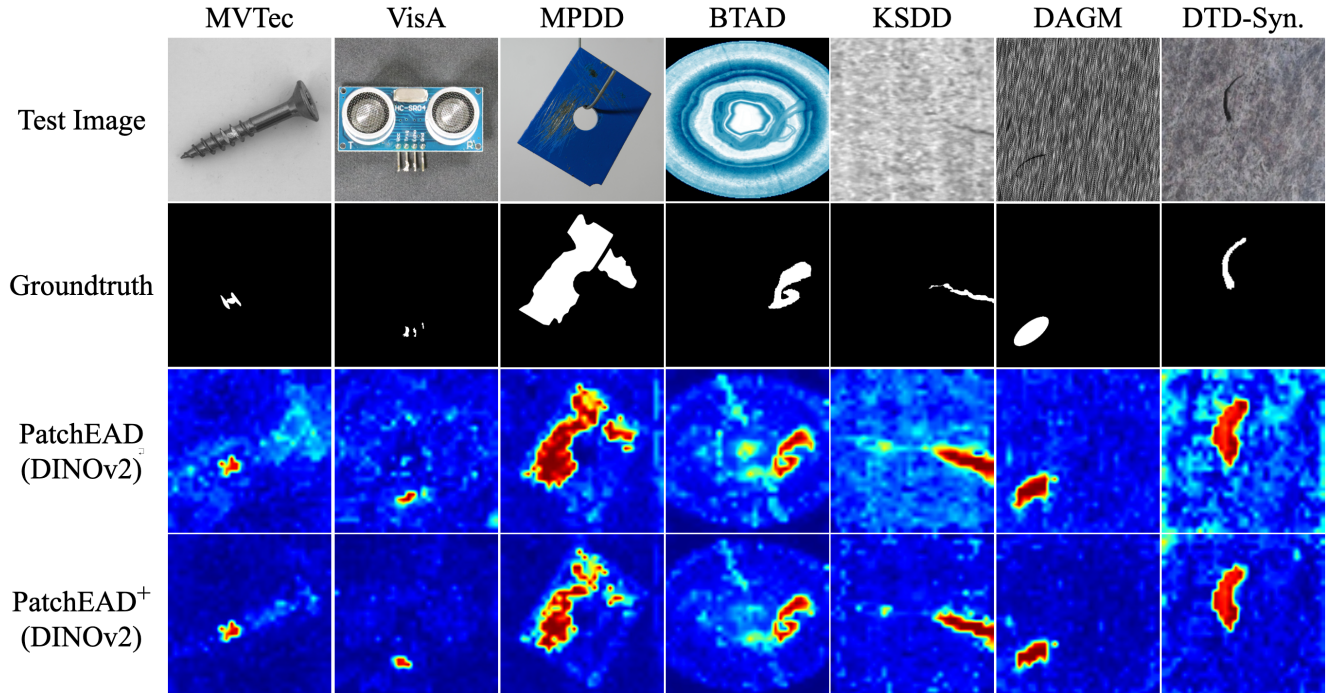


Figure 5. **Visualization of anomaly heatmaps generated by PatchEAD and PatchEAD⁺** across seven industrial datasets, showing clearer and more precise defect outlines with reduced false positives near normal regions.

tently improved accuracies with 672×672 input size for both image-level and pixel-level AUC scores. Notably, using 448×448 already produced comparable accuracy to 672×672 , offering a more efficient alternative. Larger image sizes correspond to smaller regions per patch, which may improve defect pattern recognition but increase inference time. Therefore, this parameter must balance computational efficiency with high accuracy for practical applications.

Effects of Alignment and Attention Mask: In our ablation experiments on PatchEAD⁺ using DINOv2, we evaluate the contributions of alignments and the attention mask as shown in Table 5. Results show that both components improve overall performance, and the best scores achieved when used together. Since we adopt a unified threshold setting rather than tuning attention mask thresholds for different object categories, pixel-level performance may vary and sometimes degrade depending on the object characteristics.

4.6. Anomaly Mask Visualization

Figure 5 presents visualizations of PatchEAD, highlighting their ability to reduce false positives and enhance anomaly detection accuracy. PatchEAD⁺ generates clearer and more precise defect outlines, minimizing false positives near normal regions. Further details of alignment and masking components in PatchEAD⁺ are provided in the supplementary material.

5. Conclusion

Our work demonstrates the feasibility and effectiveness of a purely vision-based, patch-centric framework for industrial anomaly detection, in contrast to recent methods that rely on text prompts. Through extensive experiments in few-shot and batch zero-shot settings, PatchEAD consistently surpasses existing baselines, achieving strong performance without additional training or external normal libraries. Furthermore, PatchEAD⁺ highlights critical design choices, such as targeted visual augmentations that stabilize the patch feature space and substantially enhance discriminative power. Importantly, our framework is backbone-agnostic, seamlessly integrating with any pre-trained vision encoder, making it immediately deployable and highly scalable across diverse industrial scenarios, and offering a practical solution for robust, real-world anomaly detection.

A limitation of our method is its reliance on visual patch information, which may miss non-visual anomalies, and small anomalous regions can produce indistinguishable patch features, reducing detection accuracy.

Future works includes refining the anomaly scoring function to better structure the feature space and enable more accurate extraction of patch-level and other nuanced information. Integrating multi-resolution techniques may further improve detection of anomalies across scales, enhancing both robustness and generalization in complex industrial settings.

References

- [1] Toshimichi Aota, Lloyd Teh Tzer Tong, and Takayuki Okatani. Zero-shot versus many-shot: Unsupervised texture anomaly detection. In *Proceedings of the IEEE/CVF Winter Conference on Applications of Computer Vision*, pages 5564–5572, 2023. 5, 1
- [2] Jaehyeok Bae, Jae-Han Lee, and Seyun Kim. PNI: Industrial anomaly detection using position and neighborhood information. In *Proceedings of the IEEE/CVF International Conference on Computer Vision*, pages 6373–6383, 2023. 1, 2
- [3] Paul Bergmann, Michael Fauser, David Sattlegger, and Carsten Steger. MVTEC AD—a comprehensive real-world dataset for unsupervised anomaly detection. In *Proceedings of the IEEE/CVF conference on computer vision and pattern recognition*, pages 9592–9600, 2019. 5, 7, 1
- [4] Paul Bergmann, Michael Fauser, David Sattlegger, and Carsten Steger. Uninformed students: Student-teacher anomaly detection with discriminative latent embeddings. In *Proceedings of the IEEE/CVF conference on computer vision and pattern recognition*, pages 4183–4192, 2020. 5
- [5] Daniel Bolya, Po-Yao Huang, Peize Sun, Jang Hyun Cho, Andrea Madotto, Chen Wei, Tengyu Ma, Jiale Zhi, Jathushan Rajasegaran, Hanoona Rasheed, et al. Perception encoder: The best visual embeddings are not at the output of the network. *arXiv preprint arXiv:2504.13181*, 2025. 7
- [6] Yunkang Cao, Xiaohao Xu, Chen Sun, Yuqi Cheng, Zongwei Du, Liang Gao, and Weiming Shen. Segment any anomaly without training via hybrid prompt regularization. *arXiv preprint arXiv:2305.10724*, 2023. 1
- [7] Yunkang Cao, Jiangning Zhang, Luca Frittoli, Yuqi Cheng, Weiming Shen, and Giacomo Boracchi. AdaCLIP: Adapting clip with hybrid learnable prompts for zero-shot anomaly detection. In *European Conference on Computer Vision*, pages 55–72. Springer, 2025. 1, 2, 5
- [8] Xuhai Chen, Yue Han, and Jiangning Zhang. A zero-/few-shot anomaly classification and segmentation method for cvpr 2023 vand workshop challenge tracks 1&2: 1st place on zero-shot ad and 4th place on few-shot ad. *arXiv preprint arXiv:2305.17382*, 2023. 2, 4, 5
- [9] Pengyu Cheng, Weituo Hao, Shuyang Dai, Jiachang Liu, Zhe Gan, and Lawrence Carin. Club: A contrastive log-ratio upper bound of mutual information. In *International conference on machine learning*, pages 1779–1788. PMLR, 2020. 2
- [10] Simon Damm, Mike Laszkiewicz, Johannes Lederer, and Asja Fischer. Anomalydino: Boosting patch-based few-shot anomaly detection with dinov2, 2025. 2
- [11] Thomas Defard, Aleksandr Setkov, Angélique Loesch, and Romaric Audigier. PaDiM: a patch distribution modeling framework for anomaly detection and localization. In *International Conference on Pattern Recognition*, pages 475–489. Springer, 2021. 1, 2, 4
- [12] Hanqiu Deng, Zhaoxiang Zhang, Jinan Bao, and Xingyu Li. AnoVL: Adapting vision-language models for unified zero-shot anomaly localization. *arXiv preprint arXiv:2308.15939*, 2023. 2
- [13] Yuxin Fang, Quan Sun, Xinggong Wang, Tiejun Huang, Xinlong Wang, and Yue Cao. EVA-02: A visual representation for neon genesis. *Image and Vision Computing*, 149:105171, 2024. 7
- [14] Zhihao Gu, Liang Liu, Xu Chen, Ran Yi, Jiangning Zhang, Yabiao Wang, Chengjie Wang, Annan Shu, Guannan Jiang, and Lizhuang Ma. Remembering normality: Memory-guided knowledge distillation for unsupervised anomaly detection. In *Proceedings of the IEEE/CVF International Conference on Computer Vision*, pages 16401–16409, 2023. 2
- [15] Zhaopeng Gu, Bingke Zhu, Guibo Zhu, Yingying Chen, Ming Tang, and Jinqiao Wang. AnomalyGPT: Detecting industrial anomalies using large vision-language models. In *Proceedings of the AAAI Conference on Artificial Intelligence*, pages 1932–1940, 2024. 2, 4
- [16] Haoyang He, Yuhu Bai, Jiangning Zhang, Qingdong He, Hongxu Chen, Zhenye Gan, Chengjie Wang, Xiangtai Li, Guanzhong Tian, and Lei Xie. MambaAD: Exploring state space models for multi-class unsupervised anomaly detection. *arXiv preprint arXiv:2404.06564*, 2024. 1, 2
- [17] Kaiming He, Xinlei Chen, Saining Xie, Yanghao Li, Piotr Dollár, and Ross Girshick. Masked autoencoders are scalable vision learners. In *Proceedings of the IEEE/CVF conference on computer vision and pattern recognition*, pages 16000–16009, 2022. 7
- [18] Jeeho Hyun, Sangyun Kim, Giyoung Jeon, Seung Hwan Kim, Kyunghoon Bae, and Byung Jun Kang. ReConPatch: Contrastive patch representation learning for industrial anomaly detection. In *Proceedings of the IEEE/CVF Winter Conference on Applications of Computer Vision*, pages 2052–2061, 2024. 1, 2
- [19] Gabriel Ilharco, Mitchell Wortsman, Ross Wightman, Cade Gordon, Nicholas Carlini, Rohan Taori, Achal Dave, Vaishaal Shankar, Hongseok Namkoong, John Miller, Hananeh Hajishirzi, Ali Farhadi, and Ludwig Schmidt. OpenCLIP, 2021. If you use this software, please cite it as below. 5, 1
- [20] Jongheon Jeong, Yang Zou, Taewan Kim, Dongqing Zhang, Avinash Ravichandran, and Onkar Dabeer. WinCLIP: Zero-/few-shot anomaly classification and segmentation. In *Proceedings of the IEEE/CVF Conference on Computer Vision and Pattern Recognition*, pages 19606–19616, 2023. 1, 2, 4, 5
- [21] Stepan Jezek, Martin Jonak, Radim Burget, Pavel Dvorak, and Milos Skotak. Deep learning-based defect detection of metal parts: evaluating current methods in complex conditions. In *2021 13th International Congress on Ultra Modern Telecommunications and Control Systems and Workshops (ICUMT)*, pages 66–71, 2021. 5, 1
- [22] Aodong Li, Chen Qiu, Marius Kloft, Padhraic Smyth, Maja Rudolph, and Stephan Mandt. Zero-shot anomaly detection via batch normalization. *Advances in Neural Information Processing Systems*, 36, 2024. 3, 6
- [23] Chun-Liang Li, Kihyuk Sohn, Jinsung Yoon, and Tomas Pfister. CutPaste: Self-supervised learning for anomaly detection and localization. In *Proceedings of the IEEE/CVF conference on computer vision and pattern recognition*, pages 9664–9674, 2021. 2

- [24] Xurui Li, Ziming Huang, Feng Xue, and Yu Zhou. MuSc: Zero-shot industrial anomaly classification and segmentation with mutual scoring of the unlabeled images. In *International Conference on Learning Representations*, 2024. 2, 3, 5, 6
- [25] Xiaofan Li, Zhizhong Zhang, Xin Tan, Chengwei Chen, Yanyun Qu, Yuan Xie, and Lizhuang Ma. PromptAD: Learning prompts with only normal samples for few-shot anomaly detection. In *Proceedings of the IEEE/CVF Conference on Computer Vision and Pattern Recognition (CVPR)*, pages 16838–16848, 2024. 2, 4, 5
- [26] Paul Pu Liang, Zihao Deng, Martin Q Ma, James Zou, Louis-Philippe Morency, and Ruslan Salakhutdinov. Factorized contrastive learning: going beyond multi-view redundancy. In *Proceedings of the 37th International Conference on Neural Information Processing Systems*, pages 32971–32998, 2023. 1
- [27] Fan Liu, Tianshu Zhang, Wenwen Dai, Chuanyi Zhang, Wenwen Cai, Xiacong Zhou, and DeLong Chen. Few-shot adaptation of multi-modal foundation models: A survey. *Artificial Intelligence Review*, 57(10):268, 2024. 1
- [28] Zhikang Liu, Yiming Zhou, Yuansheng Xu, and Zilei Wang. SimpleNet: A simple network for image anomaly detection and localization. In *Proceedings of the IEEE/CVF Conference on Computer Vision and Pattern Recognition*, pages 20402–20411, 2023. 2
- [29] Pankaj Mishra, Riccardo Verk, Daniele Fornasier, Claudio Piciarelli, and Gian Luca Foresti. VT-ADL: A vision transformer network for image anomaly detection and localization. In *30th IEEE/IES International Symposium on Industrial Electronics (ISIE)*, 2021. 5, 1
- [30] Maxime Oquab, Timothée Darcet, Theo Moutakanni, Huy V. Vo, Marc Szafraniec, Vasil Khalidov, Pierre Fernandez, Daniel Haziza, Francisco Massa, Alaaeldin El-Nouby, Russell Howes, Po-Yao Huang, Hu Xu, Vasu Sharma, Shang-Wen Li, Wojciech Galuba, Mike Rabbat, Mido Assran, Nicolas Ballas, Gabriel Synnaeve, Ishan Misra, Herve Jegou, Julien Mairal, Patrick Labatut, Armand Joulin, and Piotr Bojanowski. DINOv2: Learning robust visual features without supervision, 2023. 2, 3, 6, 7, 1
- [31] Zhiliang Peng, Li Dong, Hangbo Bao, Qixiang Ye, and Furu Wei. BEiT v2: Masked image modeling with vector-quantized visual tokenizers. *arXiv preprint arXiv:2208.06366*, 2022. 7
- [32] Zhen Qu, Xian Tao, Mukesh Prasad, Fei Shen, Zhengtao Zhang, Xinyi Gong, and Guiguang Ding. VCP-CLIP: A visual context prompting model for zero-shot anomaly segmentation. *arXiv preprint arXiv:2407.12276*, 2024. 1, 2
- [33] Alec Radford, Jong Wook Kim, Chris Hallacy, Aditya Ramesh, Gabriel Goh, Sandhini Agarwal, Girish Sastry, Amanda Askell, Pamela Mishkin, Jack Clark, et al. Learning transferable visual models from natural language supervision. In *International conference on machine learning*, pages 8748–8763. PMLR, 2021. 3, 7, 2
- [34] Karsten Roth, Latha Pemula, Joaquin Zepeda, Bernhard Schölkopf, Thomas Brox, and Peter Gehler. Towards total recall in industrial anomaly detection. In *Proceedings of the IEEE/CVF conference on computer vision and pattern recognition*, pages 14318–14328, 2022. 1, 2, 3, 4
- [35] Mohammadreza Salehi, Niousha Sadjadi, Soroosh Baselizadeh, Mohammad H Rohban, and Hamid R Rabiee. Multiresolution knowledge distillation for anomaly detection. In *Proceedings of the IEEE/CVF conference on computer vision and pattern recognition*, pages 14902–14912, 2021. 2
- [36] Oriane Siméoni, Huy V Vo, Maximilian Seitzer, Federico Baldassarre, Maxime Oquab, Cijo Jose, Vasil Khalidov, Marc Szafraniec, Seungeun Yi, Michaël Ramamonjisoa, et al. Dinov3. *arXiv preprint arXiv:2508.10104*, 2025. 7
- [37] Luc PJ Sträter, Mohammadreza Salehi, Efstratios Gavves, Cees GM Snoek, and Yuki M Asano. GeneralAD: Anomaly detection across domains by attending to distorted features. *arXiv preprint arXiv:2407.12427*, 2024. 2
- [38] Domen Tabernik, Samo Šela, Jure Skvarč, and Danijel Skočaj. Segmentation-based deep-learning approach for surface-defect detection. *Journal of Intelligent Manufacturing*, 31(3):759–776, 2020. 5, 1
- [39] Daniel Stanley Tan, Yi-Chun Chen, Trista Pei-Chun Chen, and Wei-Chao Chen. TrustMAE: A noise-resilient defect classification framework using memory-augmented auto-encoders with trust regions. In *Proceedings of the IEEE/CVF winter conference on applications of computer vision*, pages 276–285, 2021. 1, 2
- [40] Y-H Tsai, Y Wu, R Salakhutdinov, and L-P Morency. Self-supervised learning from a multi-view perspective. In *Proceedings of the International Conference on Learning Representations (ICLR), 2021*, 2021. 2
- [41] Matthias Wieler and Tobias Hahn. Weakly supervised learning for industrial optical inspection. In *DAGM symposium in*, page 11, 2007. 5, 1
- [42] Minghui Yang, Peng Wu, and Hui Feng. MemSeg: A semi-supervised method for image surface defect detection using differences and commonalities. *Engineering Applications of Artificial Intelligence*, 119:105835, 2023. 2
- [43] Zhiyuan You, Lei Cui, Yujun Shen, Kai Yang, Xin Lu, Yu Zheng, and Xinyi Le. A unified model for multi-class anomaly detection. *Advances in Neural Information Processing Systems*, 35:4571–4584, 2022. 1, 2
- [44] Vitjan Zavrtanik, Matej Kristan, and Danijel Skočaj. DRAEM -A discriminatively trained reconstruction embedding for surface anomaly detection. In *Proceedings of the IEEE/CVF international conference on computer vision*, pages 8330–8339, 2021. 1, 2
- [45] Chaoning Zhang, Fachrina Dewi Puspitasari, Sheng Zheng, Chenghao Li, Yu Qiao, Taegoo Kang, Xinru Shan, Chen-shuang Zhang, Caiyan Qin, Francois Rameau, et al. A survey on segment anything model (SAM): Vision foundation model meets prompt engineering. *arXiv preprint arXiv:2306.06211*, 2023. 1
- [46] Qihang Zhou, Guansong Pang, Yu Tian, Shibo He, and Jiming Chen. AnomalyCLIP: Object-agnostic prompt learning for zero-shot anomaly detection. In *The Twelfth International Conference on Learning Representations*, 2023. 1, 2, 5

- [47] Jiawen Zhu and Guansong Pang. Toward generalist anomaly detection via in-context residual learning with few-shot sample prompts. In *Proceedings of the IEEE/CVF Conference on Computer Vision and Pattern Recognition (CVPR)*, pages 17826–17836, 2024. [1](#), [2](#), [4](#), [5](#)
- [48] Yang Zou, Jongheon Jeong, Latha Pemula, Dongqing Zhang, and Onkar Dabeer. Spot-the-difference self-supervised pre-training for anomaly detection and segmentation. In *European Conference on Computer Vision*, pages 392–408. Springer, 2022. [5](#), [7](#), [1](#)

PatchEAD: Unifying Industrial Visual Prompting Frameworks for Patch-Exclusive Anomaly Detection

Supplementary Material

This supplementary material provides additional details to support the findings of our paper on training-free industrial anomaly detection with a patch-exclusive approach. § A includes information on the datasets used, detailing the types of multimodal data, preprocessing steps, and anomaly labeling. § B covers the architecture, feature extraction methods, and experimental setup, including hardware, software, and hyperparameters. § C introduce an information theory to analyze the information relevant to the target task (anomaly detection) and the usage under multi-modality scenario and show some experiments on text prompts compare to vision prompts. § D demonstrate the detail of our alignment and masking strategy in PatchEAD⁺. § E present the evaluation process, including metrics and baseline comparisons. § F provides visualizations that demonstrate the effectiveness of our approach in detecting anomalies. Finally, § G presents a case study to showcase the practical application of our method in a real-world industrial scenario, highlighting its performance and potential challenges.

A. Dataset Details

The experiments described in the main paper utilize seven widely recognized industrial anomaly detection datasets: MVTec [3], VisA [48], MPDD [21], BTAD [29], KSDD [38], DAGM [41], and DTD-Synthetic [1]. For datasets that provide a predefined training and testing split, we exclusively use the test data to evaluate the model’s performance. In cases where no such split is provided, we allocate 25% of the normal images and all the anomalous images as the test set. For the KSDD dataset, each image is divided into three parts to better align its aspect ratio with the other datasets. Images containing a defect are labeled as anomalous, while those without a defect are considered normal. A detailed summary of the datasets, including key characteristics and splits, is presented in Table 6.

Dataset	Type	# of Categories	Samples	
			Normal	Abnormal
MVTec [3]	Obj & Texture	15	467	1,258
VisA [48]	Obj	12	962	1,200
MPDD [21]	Obj	6	176	282
BTAD [29]	Obj	3	451	290
KSDD [38]	Texture	1	286	54
DAGM [41]	Texture	10	6,996	1,054
DTD-Synthetic [1]	Texture	12	357	947

Table 6. Anomaly Detection Datasets in Industrial Domain.

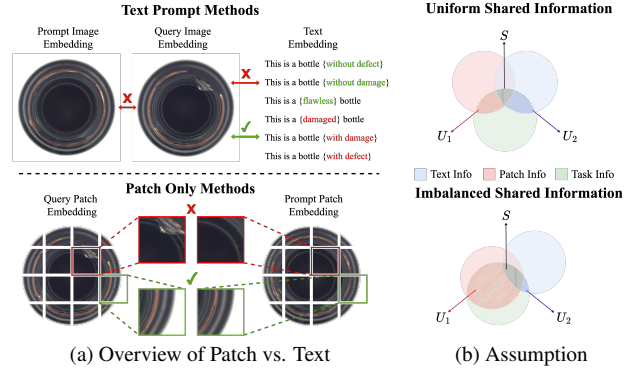


Figure 6. (a) Existing anomaly detection methods using image–text similarity often assume clean separation via simple positive/negative prompts. Our **patch-only** method detects anomalies by comparing query patches with normal prompt patches, leveraging richer context. (b) Considering shared information S and modality-unique information U_1, U_2 , task relevance varies; we argue patch-level information outweighs text information for industrial defect detection.

B. Implementation Details

Across all experiments, we adopt base-size backbones to keep parameter counts comparable. Our CLIP variant uses ViT-B-16-plus-240 pretrained on laion400m_e32 from OpenCLIP [19], with inputs resized to 240×240 to match the checkpoint. The DINOv2 variant employs dinov2_vitb14_reg from the official codebase [30] at its default 448×448 resolution. For PE_spatial, we load PE-Spatial-B16-512; for DINOv3, we use the distilled ViT-B/16. These settings keep each method close to its standard configuration and enable a fair comparison across architectures.

C. Multimodal Information Analysis

Following the formulation in [26] for handling multimodal information, we consider two input modalities, $X_i (i \in \{1, 2\})$, annotated with a label variable Y . The joint distribution of these inputs and Y can be expressed using conditional mutual information:

$$I(X_1, X_2, Y) = S + U_1 + U_2, \quad (5)$$

where $S = I(X_1; X_2; Y)$ denotes the task-relevant shared information; $U_1 = I(X_1; Y|X_2)$ and $U_2 = I(X_2; Y|X_1)$ denote the unique information of modalities X_1 and X_2 ,

respectively. Figure 6 provides a concept plot of the imbalanced shared *v.s.* unique information provided in different modalities. Our hypothesis is that patch-level information should be more important over the text information for industrial defect detection. Our aim is to uncover the imbalanced distribution of U_1 and U_2 across different modalities of texts, patches, and whole images.

Loss functions in large multi-modality models, such as CLIP [33], are often optimized to capture shared information across modalities. Consequently, other anomaly detection methods tend to add additional modules to enhance information. However, these additional modules may introduce overlapping information between modalities. Our focus is to examine the unique information provided by each modality (U_1 and U_2).

The unique information (U_1 and U_2) can be challenging to compute directly, so we approximate it using an upper-bound, I_{CLUB} , as proposed in contrastive learning [9]. When I_{CLUB} is small, the unique information in a modality is expected to be limited. For instance, we can estimate the unique information U_1 as follows:

$$U_1 = I(X_1; Y|X_2) \leq I_{CLUB}(X_1; Y|X_2), \quad (6)$$

where I_{CLUB} is given by:

$$I_{CLUB}(X_1; Y|X_2) = E[f^*(X_1, Y^+|X_2)] - E[f^*(X_1, Y^-|X_2)], \quad (7)$$

with f^* as the optimal critic from a contrastive pre-trained network. I_{CLUB} represents the expected difference between positive and negative samples, X^+ and X^- for a given X . By applying an optimal augmentation assumption [40], we replace Y with an augmented variable X' of X , assuming that only task-relevant information is shared between X and X' . I_{CLUB} can then be calculated via this adjustment as:

$$I_{CLUB}(X_1; Y|X_2) = E[f^*(X_1, X_1^+|X_2)] - E[f^*(X_1, X_1^-|X_2)]. \quad (8)$$

If the expected anomaly scores between positive and negative samples are not significantly different, this upper bound will be small, suggesting limited unique information. Minimal differences in anomaly scores may also result if X_2 provides sufficient information, thus reducing the reliance on X_1^+ and X_1^- .

Considering X_1 for the patch modality and X_2 as the text modality, we use Eq. (8) to derive the upper bounds for U_1 and U_2 . The upper bound for U_2 , $I_{CLUB}(X_2; Y|X_1)$, is expected to be small because augmenting text prompts results in minimal changes in anomaly scores once patches are already included. On the other hand, the upper bound for U_1 , $I_{CLUB}(X_1; Y|X_2)$, can be large, as augmentations

like rotation, cropping, or noise perturbations cause noticeable variations in the final anomaly scores. This larger upper bound for U_1 arises because the text prompts often fail to capture details about missing objects or defects, which are better represented in the patch modality.

C.1. Comparison of Text *vs.* Patch Information

Figure 7(a,b) compares the **normal vs. abnormal text prompts** on the MVTEC dataset. These plots explore how different prompts affect the image-text similarity score histograms for normal and abnormal samples. The information upper bound of each modality, as described in Eq. (8), is estimated based on the expected score difference between positive and negative augmentations. By comparing the distributions of scores for positive and negative prompts in panels (a) and (b), we illustrate how the text information upper bound impacts the anomaly detection performance.

Figure 7(c,d) compares the **text vs. patch modalities** by using the histogram of anomaly scores on the MVTEC dataset. (c) plots the anomaly score histogram using WinCLIP, a model featuring vision-text multimodal capability. The scores were derived from the similarity between the image and text prompt tokens. (d) plots the histogram using our PatchEAD, where only patch information is used. Observe that (d) exhibits a more separable space than (c), suggesting more discriminative results with only patch information.

Results show that the positive and negative prompts yield a highly overlapped distribution regardless of normal or abnormal images. The upper bound of text information is limited, leading to inferior discriminative power than patches.

D. Details of Alignment and Masking

We introduce both alignment and masking to MVTEC, VisA, KSSD, DAGM, and DTD-Synthetic datasets, and only masking applied on MPDD, and BTAD due to the object is well-aligned(BTAD) or 3D rotation(MPDD).

Alignment: In the few-shot setting, we calculate the displacement and rotation between each prompt image and the query image. We then add the corrected images and their 180-degree rotations to the prompt list to ensure consistent positions and angles during patch matching. In the zero-shot setting, we use the first image as the query and apply the same process to all other images. For similarity calculation, we average the scores from the three images for each sample to determine the final anomaly score.

Masking: We extract the final attention layer and average all attention heads to get the [CLS] token’s attention scores for each patch. After normalizing, patches with scores above 0.05 are set to 1, and those below to 0.5. This reduces the incorrect activations in background areas.

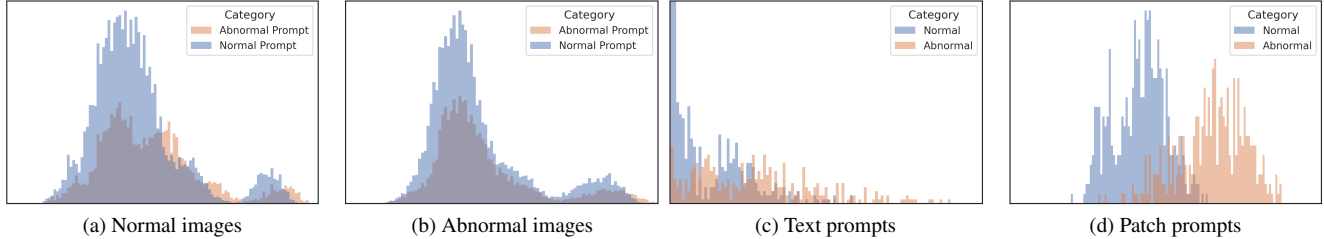


Figure 7. **Histogram plots** summarizing experimental results on the MVTec dataset. (a) and (b) depict the **image–text similarity scores** for normal and abnormal images under various text prompts. Ideally, normal images should exhibit high similarity with their corresponding normal prompts and lower similarity when paired with abnormal prompts. (c) and (d) show the **anomaly scores** computed using text and patch prompts, respectively.

E. Experimental Details

Our experiments entail few-shot and zero-shot settings with various datasets and thus only present the average results in the main manuscript under the page limitation. We report the few-shot results with each category in the MVTec and ViSA datasets in Table 7 and Table 8. The zero-shot results are reported in Table 9 using seven datasets.

When we reveal the category-wise AUC in the few-shot setting, we observe the capsule, screw, and transistor in the MVTec dataset are harder categories with lower image-level and pixel-level AUC. Using DINOv2 significantly improves PatchEAD in these categories compared to CLIP, highlighting the benefits of vision purpose pretraining for the patch-only method, even when performed in an unsupervised manner. This improvement can consistently be observed in 1-, 2-, and 4-shot results, especially on image-level AUC. PatchEAD⁺ strengthening alignment and masking mainly facilitates the screw category in different few-shot settings.

Similarly, the few-shot image-level AUC attains relatively significant improvements on specific categories such as capsules, fryum, macaroni1, and pcb2 when comparing DINOv2 and CLIP in the ViSA dataset. The improvement using PatchEAD⁺ is eminent in the fryum, macaroni1, and pcb2 categories on both image-level and pixel-level AUC over different few-shot settings. The enhanced categories are generally aligned between few-shot and zero-shot settings. Our proposed PatchEAD using only patch information complements these hard cases with delicate visual appearances.

F. Visualization Results

Additionally, to demonstrate the defect localization capability of our proposed PatchEAD framework, we conducted visualization on all test datasets. Specifically, we linearly interpolated the predicted patch anomaly scores to match the size of the original images, followed by normalization, resulting in a heatmap for each image. In the few-shot setting,

we used the MVTec and ViSA datasets for visualization, with results shown in Figures 8 and 9. In the zero-shot setting, we conducted experiments using seven datasets, with results presented in Figures 10, 11, 12, 13, 14, 15, 16. These test datasets encompass a wide variety of object types, and the visualization results indicate that our method, even without training, can accurately localize various defects under different settings, demonstrating the framework’s strong flexibility and generalization capability.

G. Case Study

We conducted a visual comparison to evaluate the effectiveness of alignment and masking in our method. As shown in Figure 17, masking reduces the weight of background regions, thereby decreasing the likelihood of misclassification. Meanwhile, alignment addresses variations in object orientation and displacement by aligning objects, enabling the comparison of similar contours and significantly reducing misclassification at object edges.

Category	Image-Level AUC				Pixel-Level AUC			
	PatchEAD	PatchEAD	PatchEAD+	PatchEAD+	PatchEAD	PatchEAD	PatchEAD+	PatchEAD+
	ViT-B/16+	DINOv2-B	ViT-B/16+	DINOv2-B	ViT-B/16+	DINOv2-B	ViT-B/16+	DINOv2-B
1-shot								
bottle	98.2 \pm 0.7	98.8 \pm 1.6	98.5 \pm 0.7	99.7 \pm 0.4	97.9 \pm 0.1	98.3 \pm 0.1	98.0 \pm 0.1	98.1 \pm 0.1
cable	90.4 \pm 2.0	90.8 \pm 1.9	88.8 \pm 2.0	92.5 \pm 1.1	93.9 \pm 0.4	93.2 \pm 0.5	93.9 \pm 0.3	93.4 \pm 0.4
capsule	80.8 \pm 12.0	82.4 \pm 13.3	78.2 \pm 11.8	85.9 \pm 11.2	90.6 \pm 0.7	97.4 \pm 0.2	93.4 \pm 0.6	98.0 \pm 0.2
carpet	99.9 \pm 0.1	98.5 \pm 1.4	100.0 \pm 0.0	99.6 \pm 0.3	99.3 \pm 0.1	98.7 \pm 0.1	99.3 \pm 0.0	98.7 \pm 0.1
grid	99.4 \pm 0.5	99.1 \pm 0.6	99.7 \pm 0.2	97.7 \pm 0.6	98.2 \pm 0.1	98.7 \pm 0.1	98.2 \pm 0.1	98.7 \pm 0.2
hazelnut	99.4 \pm 0.2	98.6 \pm 0.8	99.7 \pm 0.2	99.4 \pm 0.3	98.8 \pm 0.2	98.9 \pm 0.1	98.2 \pm 0.1	99.4 \pm 0.0
leather	100.0 \pm 0.0	99.8 \pm 0.2	100.0 \pm 0.0	100.0 \pm 0.0	99.3 \pm 0.0	98.8 \pm 0.1	99.4 \pm 0.0	99.0 \pm 0.1
metal_nut	99.9 \pm 0.1	98.8 \pm 0.9	98.3 \pm 0.3	99.7 \pm 0.2	87.2 \pm 0.5	95.8 \pm 0.4	90.5 \pm 0.3	95.4 \pm 0.5
pill	96.3 \pm 0.2	91.4 \pm 5.1	93.8 \pm 0.6	93.7 \pm 3.6	93.8 \pm 0.4	93.8 \pm 0.6	93.0 \pm 0.5	94.1 \pm 0.7
screw	62.8 \pm 5.5	77.4 \pm 4.2	78.5 \pm 1.3	80.6 \pm 3.7	92.5 \pm 0.9	97.2 \pm 0.2	94.8 \pm 0.6	97.9 \pm 0.1
tile	99.5 \pm 0.3	99.8 \pm 0.1	98.4 \pm 0.7	100.0 \pm 0.0	95.4 \pm 0.2	94.4 \pm 0.2	95.4 \pm 0.1	95.0 \pm 0.2
toothbrush	95.2 \pm 1.0	94.0 \pm 4.4	94.9 \pm 0.9	94.4 \pm 3.1	97.7 \pm 0.3	98.8 \pm 0.2	98.1 \pm 0.2	98.2 \pm 0.3
transistor	75.6 \pm 7.5	76.3 \pm 7.0	81.5 \pm 4.6	82.0 \pm 6.1	86.7 \pm 1.7	86.7 \pm 1.4	84.5 \pm 1.7	85.8 \pm 1.5
wood	98.8 \pm 0.4	99.3 \pm 0.2	99.1 \pm 0.4	100.0 \pm 0.0	95.2 \pm 0.2	92.1 \pm 0.9	94.9 \pm 0.2	93.4 \pm 1.0
zipper	94.1 \pm 1.0	99.2 \pm 0.2	92.2 \pm 1.5	99.7 \pm 0.1	90.7 \pm 0.8	96.9 \pm 0.4	91.9 \pm 0.4	97.1 \pm 0.3
Average	92.8 \pm 0.9	93.6 \pm 0.7	93.4 \pm 0.8	95.0 \pm 0.6	94.6 \pm 0.2	96.0 \pm 0.1	94.9 \pm 0.2	96.1 \pm 0.2
2-shot								
bottle	98.7 \pm 0.8	99.2 \pm 1.2	98.9 \pm 0.7	99.8 \pm 0.4	97.9 \pm 0.1	98.4 \pm 0.1	98.0 \pm 0.1	98.1 \pm 0.1
cable	91.4 \pm 2.2	91.6 \pm 2.0	90.0 \pm 2.5	93.3 \pm 1.7	94.3 \pm 0.5	93.8 \pm 0.7	94.3 \pm 0.6	93.9 \pm 0.5
capsule	76.5 \pm 11.8	85.2 \pm 10.4	74.1 \pm 11.3	86.6 \pm 8.3	90.6 \pm 0.6	97.6 \pm 0.2	93.2 \pm 0.7	98.1 \pm 0.2
carpet	99.9 \pm 0.1	99.0 \pm 1.1	100.0 \pm 0.0	99.6 \pm 0.4	99.3 \pm 0.1	98.7 \pm 0.0	99.2 \pm 0.0	98.7 \pm 0.1
grid	99.1 \pm 0.6	99.4 \pm 0.5	99.4 \pm 0.4	98.0 \pm 0.5	98.1 \pm 0.2	99.0 \pm 0.1	98.2 \pm 0.1	98.9 \pm 0.2
hazelnut	99.3 \pm 0.4	97.6 \pm 2.0	99.7 \pm 0.2	98.7 \pm 1.3	98.8 \pm 0.1	99.5 \pm 0.1	98.5 \pm 0.1	99.4 \pm 0.0
leather	100.0 \pm 0.0	99.9 \pm 0.2	100.0 \pm 0.0	100.0 \pm 0.0	99.3 \pm 0.0	98.7 \pm 0.1	99.4 \pm 0.0	98.9 \pm 0.1
metal_nut	100.0 \pm 0.1	98.8 \pm 0.6	99.0 \pm 0.8	99.9 \pm 0.2	88.5 \pm 1.5	96.4 \pm 0.7	91.6 \pm 1.2	96.0 \pm 0.8
pill	96.4 \pm 0.4	91.6 \pm 3.7	93.7 \pm 0.6	94.0 \pm 2.6	94.2 \pm 0.4	94.4 \pm 0.8	93.3 \pm 0.5	94.7 \pm 0.8
screw	67.3 \pm 6.4	79.4 \pm 3.7	79.5 \pm 1.5	84.3 \pm 4.7	92.9 \pm 1.2	97.5 \pm 0.3	95.2 \pm 0.6	98.0 \pm 0.2
tile	99.6 \pm 0.3	99.9 \pm 0.1	98.7 \pm 0.7	100.0 \pm 0.0	95.5 \pm 0.1	94.5 \pm 0.2	95.4 \pm 0.1	95.1 \pm 0.1
toothbrush	96.2 \pm 1.3	96.0 \pm 3.7	95.5 \pm 1.0	96.8 \pm 3.3	97.9 \pm 0.3	99.0 \pm 0.3	98.3 \pm 0.3	98.4 \pm 0.4
transistor	75.6 \pm 7.0	77.8 \pm 8.0	80.7 \pm 5.3	83.0 \pm 7.8	86.6 \pm 1.8	86.2 \pm 2.2	84.4 \pm 2.0	85.3 \pm 2.3
wood	98.6 \pm 0.5	99.5 \pm 0.3	99.0 \pm 0.4	100.0 \pm 0.0	95.3 \pm 0.2	92.4 \pm 0.8	95.0 \pm 0.2	93.7 \pm 0.9
zipper	92.7 \pm 4.0	99.4 \pm 0.3	90.7 \pm 6.4	99.7 \pm 0.1	90.6 \pm 0.7	96.7 \pm 0.4	92.0 \pm 0.5	97.0 \pm 0.3
Average	92.8 \pm 0.5	95.0 \pm 0.0	93.1 \pm 0.4	96.2 \pm 0.4	94.8 \pm 0.1	96.3 \pm 0.1	95.2 \pm 0.2	96.4 \pm 0.1
4-shot								
bottle	99.0 \pm 0.8	99.5 \pm 1.1	99.1 \pm 0.7	99.9 \pm 0.3	97.9 \pm 0.1	98.5 \pm 0.1	98.0 \pm 0.1	98.2 \pm 0.1
cable	92.0 \pm 2.2	92.1 \pm 1.9	90.7 \pm 2.4	93.9 \pm 1.7	94.5 \pm 0.6	94.0 \pm 0.7	94.5 \pm 0.6	94.1 \pm 0.6
capsule	78.6 \pm 12.5	84.2 \pm 11.3	76.0 \pm 12.2	86.1 \pm 9.3	90.8 \pm 0.8	97.7 \pm 0.3	93.3 \pm 0.8	98.2 \pm 0.2
carpet	99.9 \pm 0.2	99.1 \pm 1.0	100.0 \pm 0.1	99.6 \pm 0.4	99.3 \pm 0.1	98.8 \pm 0.1	99.3 \pm 0.0	98.8 \pm 0.1
grid	99.0 \pm 0.5	99.6 \pm 0.5	99.4 \pm 0.2	98.2 \pm 0.5	98.2 \pm 0.2	98.8 \pm 0.3	98.3 \pm 0.1	98.9 \pm 0.2
hazelnut	99.5 \pm 0.5	98.2 \pm 1.9	99.8 \pm 0.2	99.1 \pm 1.2	98.8 \pm 0.1	99.5 \pm 0.1	98.5 \pm 0.1	99.4 \pm 0.1
leather	100.0 \pm 0.0	99.9 \pm 0.2	100.0 \pm 0.0	100.0 \pm 0.0	99.3 \pm 0.1	99.5 \pm 0.1	99.4 \pm 0.0	98.9 \pm 0.1
metal_nut	100.0 \pm 0.0	99.0 \pm 0.6	99.4 \pm 0.8	99.9 \pm 0.2	89.5 \pm 2.0	96.8 \pm 0.8	92.4 \pm 1.5	96.5 \pm 0.9
pill	96.4 \pm 0.4	92.5 \pm 3.3	93.9 \pm 0.8	94.7 \pm 2.4	94.5 \pm 0.6	94.7 \pm 0.8	93.7 \pm 0.7	95.0 \pm 0.8
screw	71.3 \pm 7.7	81.5 \pm 4.5	80.6 \pm 2.4	86.2 \pm 5.0	93.8 \pm 1.6	97.8 \pm 0.5	95.6 \pm 0.7	98.2 \pm 0.3
tile	99.7 \pm 0.3	99.9 \pm 0.1	99.0 \pm 0.8	100.0 \pm 0.0	95.5 \pm 0.2	94.5 \pm 0.2	95.5 \pm 0.2	95.1 \pm 0.2
toothbrush	96.3 \pm 1.1	96.2 \pm 3.4	95.7 \pm 1.2	97.0 \pm 3.0	97.9 \pm 0.3	99.0 \pm 0.2	98.3 \pm 0.2	98.4 \pm 0.3
transistor	80.0 \pm 8.5	82.1 \pm 9.1	83.7 \pm 6.2	86.4 \pm 8.0	87.9 \pm 2.4	87.4 \pm 2.5	85.9 \pm 2.7	86.6 \pm 2.7
wood	98.3 \pm 0.8	99.6 \pm 0.3	98.9 \pm 0.3	100.0 \pm 0.0	95.3 \pm 0.2	92.3 \pm 0.7	95.1 \pm 0.2	93.6 \pm 0.8
zipper	93.6 \pm 3.5	99.5 \pm 0.3	92.3 \pm 5.7	99.8 \pm 0.1	90.9 \pm 0.9	97.0 \pm 0.5	92.3 \pm 0.7	97.3 \pm 0.4
Average	95.2 \pm 0.9	96.0 \pm 1.2	95.2 \pm 0.8	97.0 \pm 0.8	95.6 \pm 0.1	96.8 \pm 0.1	95.9 \pm 0.1	96.9 \pm 0.1

Table 7. Comparison of image-level and pixel-level AUC for each category in MVTec using training-free few-shot methods.

Category	Image-Level AUC				Pixel-Level AUC			
	PatchEAD	PatchEAD	PatchEAD+	PatchEAD+	PatchEAD	PatchEAD	PatchEAD+	PatchEAD+
	ViT-B/16+	DINOV2-B	ViT-B/16+	DINOV2-B	ViT-B/16+	DINOV2-B	ViT-B/16+	DINOV2-B
1-shot								
candle	92.0 \pm 1.6	86.2 \pm 3.6	94.8 \pm 1.0	90.7 \pm 1.1	96.8 \pm 0.0	98.7 \pm 0.1	97.0 \pm 0.1	98.7 \pm 0.1
capsules	79.2 \pm 1.1	95.7 \pm 0.6	80.5 \pm 2.4	93.1 \pm 0.3	94.7 \pm 0.3	97.3 \pm 0.1	95.4 \pm 0.1	96.7 \pm 0.1
cashew	92.4 \pm 1.5	86.2 \pm 1.8	93.4 \pm 1.4	90.5 \pm 1.1	97.0 \pm 0.3	99.0 \pm 0.1	97.5 \pm 0.1	98.4 \pm 0.1
chewinggum	97.4 \pm 0.0	98.2 \pm 0.7	97.9 \pm 0.1	98.7 \pm 0.1	98.7 \pm 0.1	99.4 \pm 0.0	98.9 \pm 0.1	99.4 \pm 0.0
fryum	93.7 \pm 2.3	94.2 \pm 1.0	92.6 \pm 1.5	95.7 \pm 1.0	91.0 \pm 0.7	92.7 \pm 0.2	93.1 \pm 0.4	93.8 \pm 0.3
macaroni1	85.1 \pm 3.1	88.6 \pm 2.2	91.1 \pm 0.8	92.3 \pm 1.1	96.7 \pm 0.4	99.2 \pm 0.0	97.6 \pm 0.3	99.3 \pm 0.0
macaroni2	63.5 \pm 4.1	62.9 \pm 3.9	73.3 \pm 2.4	67.4 \pm 2.9	91.2 \pm 0.9	96.9 \pm 0.2	94.6 \pm 0.1	98.3 \pm 0.1
pcb1	66.3 \pm 17.8	75.6 \pm 4.8	79.7 \pm 8.6	82.1 \pm 7.0	95.6 \pm 1.1	99.0 \pm 0.0	98.0 \pm 0.3	99.0 \pm 0.0
pcb2	74.9 \pm 2.9	75.0 \pm 3.5	72.7 \pm 3.4	82.3 \pm 3.7	92.2 \pm 0.3	95.7 \pm 0.4	92.8 \pm 0.3	95.9 \pm 0.4
pcb3	79.7 \pm 4.6	77.5 \pm 0.8	73.5 \pm 5.6	86.8 \pm 1.5	93.3 \pm 0.6	96.7 \pm 0.2	93.4 \pm 0.7	96.2 \pm 0.2
pcb4	90.6 \pm 4.3	87.2 \pm 1.4	85.5 \pm 4.3	93.1 \pm 1.3	89.8 \pm 1.0	94.4 \pm 0.6	92.1 \pm 0.8	94.7 \pm 0.6
pipe.fryum	99.4 \pm 0.2	97.6 \pm 0.9	99.6 \pm 0.2	95.8 \pm 0.7	97.0 \pm 0.4	98.7 \pm 0.1	96.6 \pm 0.6	97.9 \pm 0.2
Average	84.5 \pm 1.3	85.4 \pm 0.3	86.2 \pm 0.6	89.1 \pm 0.4	94.5 \pm 0.2	97.3 \pm 0.1	95.6 \pm 0.1	97.4 \pm 0.1
2-shot								
candle	92.2 \pm 1.4	88.9 \pm 3.7	94.6 \pm 1.1	91.7 \pm 1.4	97.0 \pm 0.2	98.8 \pm 0.2	97.2 \pm 0.2	98.8 \pm 0.2
capsules	79.8 \pm 1.8	96.0 \pm 1.3	80.7 \pm 2.6	93.1 \pm 0.6	94.7 \pm 0.3	97.3 \pm 0.3	95.4 \pm 0.2	96.7 \pm 0.3
cashew	92.7 \pm 1.7	87.8 \pm 2.8	94.6 \pm 1.7	91.6 \pm 1.7	97.2 \pm 0.3	99.1 \pm 0.1	97.6 \pm 0.2	98.6 \pm 0.2
chewinggum	97.1 \pm 0.5	97.9 \pm 0.7	97.5 \pm 0.5	98.7 \pm 0.2	98.7 \pm 0.1	99.4 \pm 0.1	98.8 \pm 0.1	99.3 \pm 0.0
fryum	94.7 \pm 1.9	95.5 \pm 1.5	93.0 \pm 1.2	96.8 \pm 1.3	91.6 \pm 0.8	93.4 \pm 0.7	93.5 \pm 0.5	94.3 \pm 0.6
macaroni1	87.1 \pm 3.6	88.9 \pm 1.9	90.4 \pm 1.7	92.9 \pm 1.2	97.1 \pm 0.8	99.3 \pm 0.1	97.8 \pm 0.6	99.4 \pm 0.1
macaroni2	71.6 \pm 8.7	66.5 \pm 4.9	76.8 \pm 3.9	69.6 \pm 3.2	92.9 \pm 1.9	97.3 \pm 0.5	95.3 \pm 0.8	98.6 \pm 0.3
pcb1	73.8 \pm 15.0	76.7 \pm 3.6	81.7 \pm 6.9	83.5 \pm 5.4	96.8 \pm 1.4	99.1 \pm 0.1	98.3 \pm 0.4	99.1 \pm 0.1
pcb2	74.5 \pm 2.7	75.7 \pm 4.1	71.4 \pm 3.3	83.2 \pm 3.2	92.9 \pm 0.8	96.2 \pm 0.6	93.3 \pm 0.7	96.4 \pm 0.6
pcb3	83.3 \pm 5.0	80.1 \pm 3.5	77.1 \pm 5.5	87.5 \pm 1.9	93.7 \pm 0.6	96.8 \pm 0.2	93.9 \pm 0.7	96.3 \pm 0.2
pcb4	87.4 \pm 12.4	87.3 \pm 1.2	85.2 \pm 11.1	93.3 \pm 1.2	90.9 \pm 1.4	94.5 \pm 0.5	92.9 \pm 1.1	94.9 \pm 0.5
pipe.fryum	99.5 \pm 0.2	97.5 \pm 0.7	99.7 \pm 0.2	95.9 \pm 0.5	97.2 \pm 0.5	98.7 \pm 0.1	96.8 \pm 0.6	98.0 \pm 0.2
Average	87.8 \pm 1.4	87.7 \pm 0.3	87.6 \pm 1.2	90.6 \pm 0.5	95.6 \pm 0.1	97.7 \pm 0.1	96.2 \pm 0.1	97.7 \pm 0.1
4-shot								
candle	92.9 \pm 1.7	90.2 \pm 3.6	94.9 \pm 1.2	92.3 \pm 1.5	97.2 \pm 0.4	98.9 \pm 0.2	97.4 \pm 0.4	98.9 \pm 0.2
capsules	80.5 \pm 2.2	96.2 \pm 1.1	81.6 \pm 2.5	93.4 \pm 0.7	95.0 \pm 0.6	97.4 \pm 0.3	95.7 \pm 0.5	96.8 \pm 0.3
cashew	92.8 \pm 1.9	88.5 \pm 2.6	94.7 \pm 1.6	92.3 \pm 1.7	97.2 \pm 0.3	99.1 \pm 0.2	97.6 \pm 0.2	98.6 \pm 0.2
chewinggum	97.5 \pm 0.7	98.2 \pm 0.7	97.6 \pm 0.5	98.7 \pm 0.3	98.7 \pm 0.1	99.4 \pm 0.0	98.8 \pm 0.1	99.3 \pm 0.0
fryum	95.1 \pm 1.7	95.9 \pm 1.5	93.6 \pm 1.4	97.0 \pm 1.1	92.2 \pm 1.0	93.8 \pm 0.9	94.0 \pm 0.8	94.7 \pm 0.7
macaroni1	87.3 \pm 3.0	89.1 \pm 1.7	90.3 \pm 1.4	93.2 \pm 1.1	97.2 \pm 0.7	99.4 \pm 0.1	97.9 \pm 0.5	99.4 \pm 0.1
macaroni2	73.0 \pm 7.5	67.6 \pm 4.4	77.0 \pm 3.2	70.8 \pm 3.8	93.6 \pm 1.9	97.5 \pm 0.5	95.4 \pm 0.7	98.7 \pm 0.3
pcb1	78.8 \pm 14.2	79.1 \pm 4.8	84.4 \pm 7.0	85.9 \pm 5.8	97.1 \pm 1.3	99.2 \pm 0.1	98.5 \pm 0.4	99.2 \pm 0.1
pcb2	76.6 \pm 4.1	77.9 \pm 4.7	74.5 \pm 5.3	84.7 \pm 3.4	93.5 \pm 1.1	96.5 \pm 0.7	93.9 \pm 1.0	96.7 \pm 0.7
pcb3	84.7 \pm 4.6	80.4 \pm 2.9	80.0 \pm 6.1	88.2 \pm 1.9	94.1 \pm 0.7	97.1 \pm 0.4	94.4 \pm 0.8	96.5 \pm 0.4
pcb4	87.3 \pm 10.3	87.6 \pm 1.1	84.5 \pm 9.2	93.6 \pm 1.1	91.8 \pm 1.8	94.9 \pm 0.6	93.6 \pm 1.3	95.2 \pm 0.6
pipe.fryum	99.6 \pm 0.2	97.5 \pm 1.0	99.8 \pm 0.2	96.2 \pm 0.9	97.3 \pm 0.4	98.8 \pm 0.1	96.9 \pm 0.5	98.1 \pm 0.2
Average	89.3 \pm 0.5	88.9 \pm 0.0	89.5 \pm 0.3	91.9 \pm 0.3	96.1 \pm 0.1	98.0 \pm 0.0	96.7 \pm 0.1	98.0 \pm 0.0

Table 8. Comparison of image-level and pixel-level AUC for each category in VisA using training-free few-shot methods.

Category	Image-Level AUC				Pixel-Level AUC			
	PatchEAD	PatchEAD	PatchEAD+	PatchEAD+	PatchEAD	PatchEAD	PatchEAD+	PatchEAD+
	ViT-B/16+	DINOv2-B	ViT-B/16+	DINOv2-B	ViT-B/16+	DINOv2-B	ViT-B/16+	DINOv2-B
MVTec								
bottle	98.7	99.5	97.7	99.8	98.2	98.7	98.2	97.9
cable	93.5	96.4	92.4	95.1	95.2	95.3	94.3	93.0
capsule	88.0	86.9	91.1	89.1	92.8	97.7	92.1	98.5
carpet	98.2	98.6	99.1	99.9	98.9	98.3	99.0	98.6
grid	98.5	90.1	93.9	99.7	97.9	98.6	97.8	99.0
hazelnut	98.2	90.2	98.2	95.1	99.1	99.4	99.1	99.3
leather	99.4	95.1	96.9	100.0	98.9	98.5	99.0	99.3
metal_nut	95.4	96.2	97.1	95.4	79.4	87.6	78.4	85.4
pill	95.2	95.2	95.2	95.6	95.0	93.0	94.9	95.2
screw	80.9	81.1	82.5	87.0	97.0	97.0	93.6	97.3
tile	100.0	100.0	99.8	99.8	96.0	96.7	95.6	95.9
toothbrush	100.0	100.0	99.2	98.9	98.4	98.8	98.4	97.4
transistor	89.4	91.9	90.0	92.7	91.3	92.5	89.7	88.9
wood	92.2	93.9	94.9	97.3	96.1	92.8	96.0	91.0
zipper	90.3	98.7	91.3	93.9	90.1	93.2	90.1	97.1
Average	94.5	94.3	<u>94.6</u>	95.9	95.0	95.9	94.4	<u>95.6</u>
VisA								
candle	93.1	90.8	93.3	89.8	97.7	98.2	97.7	99.0
capsules	80.7	92.5	81.7	94.6	96.2	96.0	95.7	97.0
cashew	86.0	88.7	84.3	93.7	97.9	99.4	97.7	98.5
chewinggum	97.7	97.7	98.1	98.8	98.5	98.8	98.6	99.0
fryum	95.6	92.7	92.3	96.0	94.1	92.7	93.1	94.6
macaroni1	87.5	85.3	90.8	96.7	98.0	98.5	98.0	99.5
macaroni2	75.3	67.2	76.2	82.4	95.6	97.5	95.6	98.9
pcb1	81.3	79.5	82.9	88.9	98.2	99.0	98.4	99.3
pcb2	81.4	81.6	81.7	87.3	95.0	95.8	95.0	97.2
pcb3	88.2	91.2	90.5	88.2	95.5	96.8	95.2	96.6
pcb4	78.3	87.9	75.0	93.8	93.3	90.9	92.6	94.8
pipe_fryum	96.8	94.5	96.4	96.4	97.9	99.0	97.8	98.0
Average	86.8	<u>87.5</u>	86.9	92.2	96.5	<u>96.9</u>	96.3	97.7
MPDD								
bracket_black	50.9	46.3	53.4	45.8	89.8	95.3	91.4	96.6
bracket_brown	50.5	50.7	51.7	59.7	93.8	94.0	93.8	94.3
bracket_white	43.1	35.7	45.0	43.2	92.2	97.6	92.8	98.6
connector	90.4	77.7	90.5	79.5	97.5	97.7	97.6	97.7
metal_plate	90.4	88.6	91.5	88.4	92.2	91.9	91.7	93.1
tubes	91.7	92.9	91.7	94.9	98.5	98.8	98.6	99.2
Average	<u>69.5</u>	65.3	70.6	68.6	94.0	<u>95.9</u>	94.3	96.6

Table 9. Comparison of image-level and pixel-level AUC for each category in MVTec, VisA, and MPDD using training-free zero-shot methods.

Category	Image-Level AUC				Pixel-Level AUC			
	PatchEAD	PatchEAD	PatchEAD+	PatchEAD+	PatchEAD	PatchEAD	PatchEAD+	PatchEAD+
	ViT-B/16+	DINOv2-B	ViT-B/16+	DINOv2-B	ViT-B/16+	DINOv2-B	ViT-B/16+	DINOv2-B
BTAD								
01	96.4	95.7	93.5	94.1	95.3	97.3	95.3	97.0
02	81.0	82.2	81.7	81.4	94.6	95.3	95.0	94.4
03	99.5	99.2	99.2	98.1	99.4	99.6	99.4	99.5
Average	92.3	92.3	91.5	91.2	96.4	97.4	96.5	<u>97.0</u>
KSDD								
KSDD	89.0	93.7	89.4	97.0	97.6	<u>99.2</u>	97.7	99.3
Average	89.0	<u>93.7</u>	89.4	97.0	97.6	<u>99.2</u>	97.7	99.3
DAGM								
Class1	78.2	85.1	83.6	88.3	86.7	80.8	87.5	76.2
Class2	99.4	100.0	99.6	99.8	99.2	99.8	99.2	99.6
Class3	97.1	99.6	95.3	99.9	95.3	97.8	95.7	97.3
Class4	100.0	100.0	100.0	100.0	99.2	97.1	99.0	95.8
Class5	97.7	99.9	98.8	100.0	96.0	99.8	96.1	99.7
Class6	91.6	100.0	95.3	100.0	91.6	99.6	92.1	99.5
Class7	99.9	100.0	100.0	100.0	95.9	97.8	95.7	96.8
Class8	82.4	99.8	83.7	99.0	93.1	99.7	93.5	99.7
Class9	78.5	91.6	87.3	95.9	92.2	99.6	95.0	99.9
Class10	100.0	100.0	99.8	100.0	99.6	99.7	99.6	99.3
Average	92.5	<u>97.6</u>	94.3	98.3	94.9	97.2	95.3	<u>96.4</u>
DTD-Synthetic								
Blotchy_099	93.7	94.1	97.6	99.3	99.0	97.8	99.0	99.0
Fibrous_183	97.6	90.4	98.1	96.7	98.7	98.7	98.6	99.1
Marbled_078	86.0	88.6	86.7	97.4	96.9	96.2	96.0	97.9
Matted_069	75.7	73.1	76.5	92.2	95.4	94.2	95.1	98.7
Mesh_114	88.2	95.6	87.4	95.9	97.7	98.4	97.1	97.1
Perforated_037	97.3	94.0	98.4	98.3	99.2	99.0	99.1	98.7
Stratified_154	90.6	98.5	84.9	98.8	99.2	99.3	99.2	99.8
Woven_001	98.9	97.5	98.5	99.6	99.4	99.8	99.2	99.8
Woven_068	94.4	91.3	94.5	95.4	98.7	98.7	98.3	98.1
Woven_104	96.5	85.5	90.9	98.9	97.2	97.4	97.6	98.6
Woven_125	94.9	91.8	94.2	99.2	99.0	99.0	98.8	98.5
Woven_127	95.1	95.9	94.7	99.0	94.2	95.7	94.3	94.9
Average	<u>92.4</u>	91.4	91.9	97.6	<u>97.9</u>	<u>97.9</u>	97.7	98.3

Table 10. Comparison of image-level and pixel-level AUC for each category in BTAD, KSDD, DAGM, and DTD-Synthetic using training-free zero-shot methods.

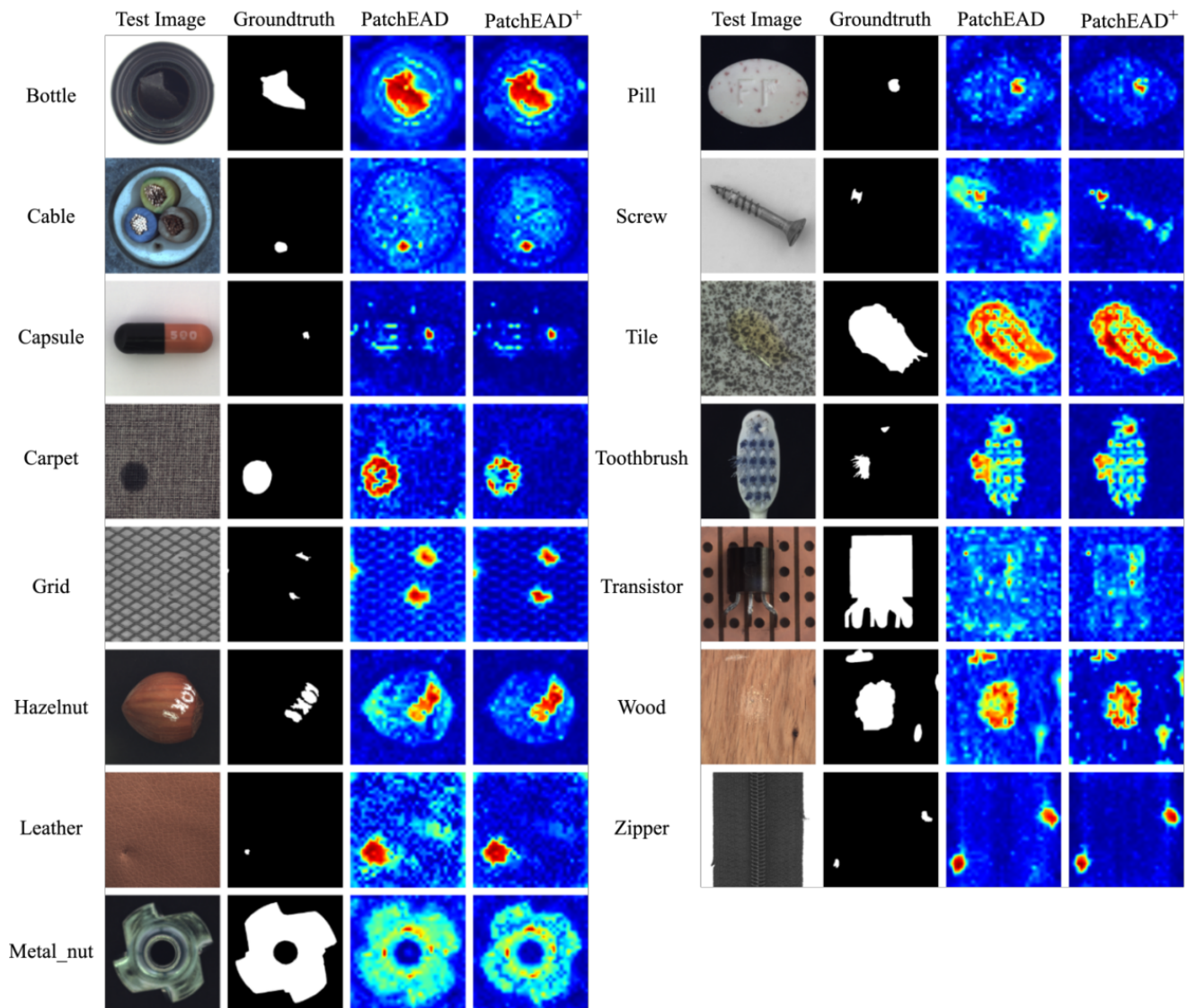


Figure 8. Additional visualization results from PatchEAD and PatchEAD+(4-shot), tested on MVTec.

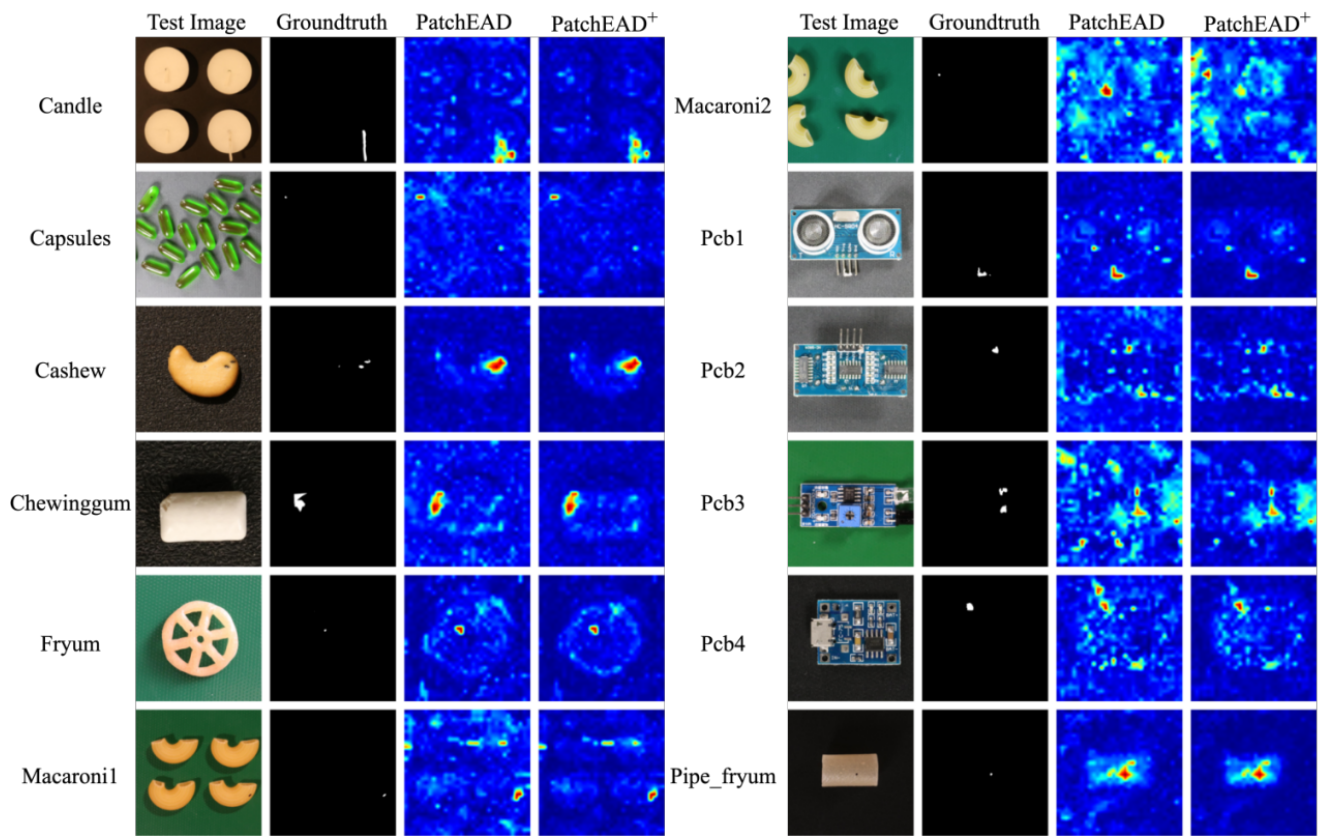


Figure 9. Additional visualization results from PatchEAD and PatchEAD+(4-shot), tested on VisA.

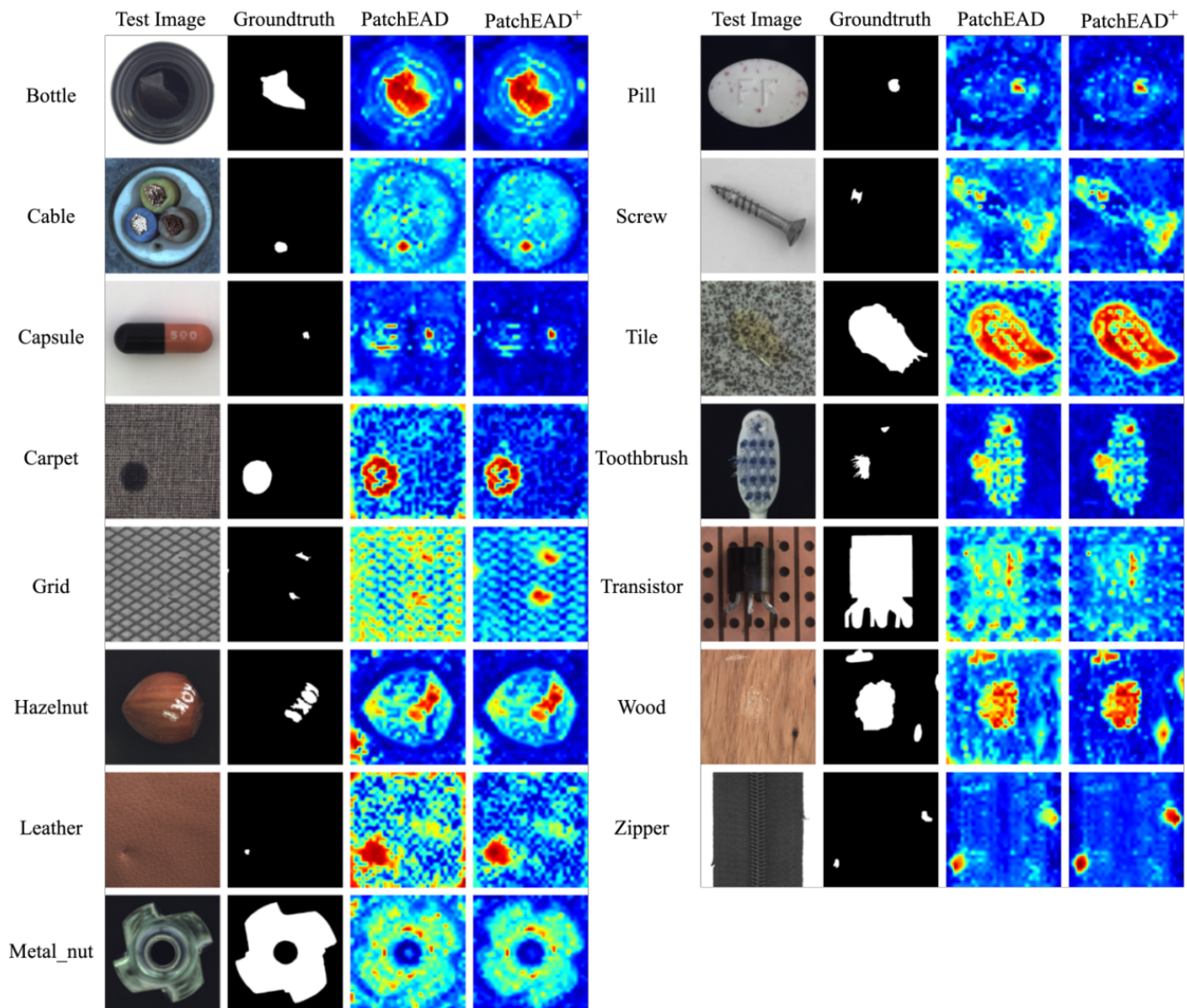


Figure 10. Additional visualization results from PatchEAD and PatchEAD+(0-shot), tested on MVTec.

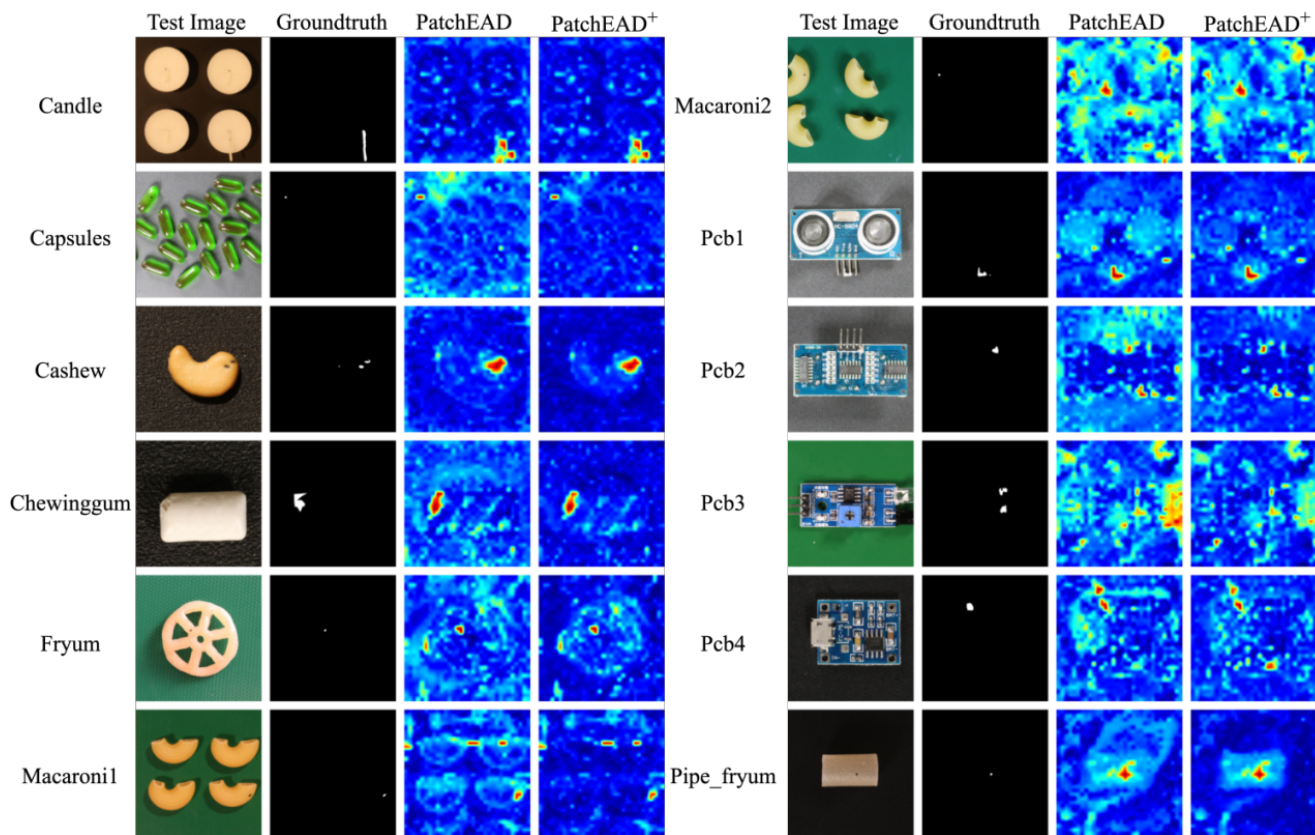


Figure 11. Additional visualization results from PatchEAD and PatchEAD+(0-shot), tested on VisA.

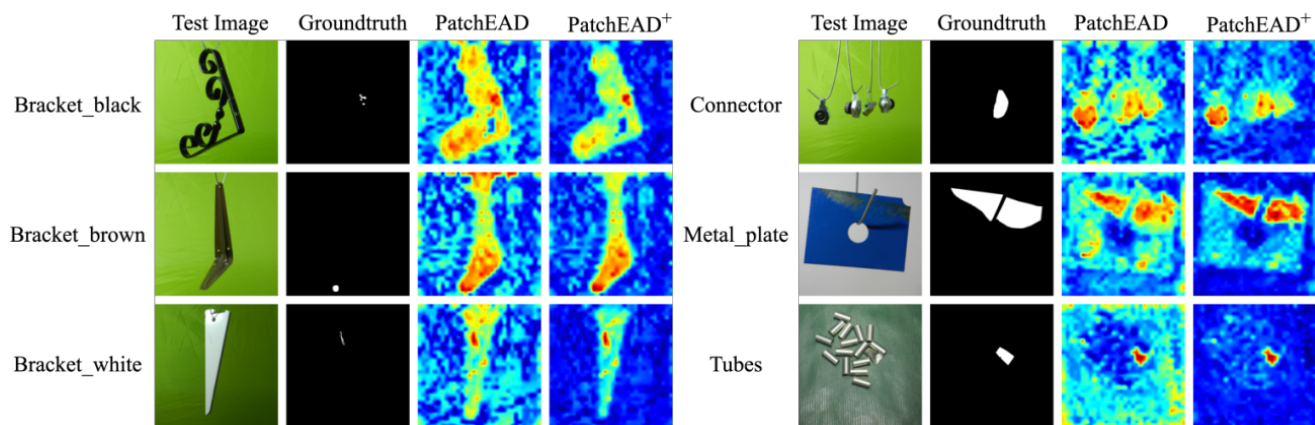


Figure 12. Additional visualization results from PatchEAD and PatchEAD+(0-shot), tested on MPDD.

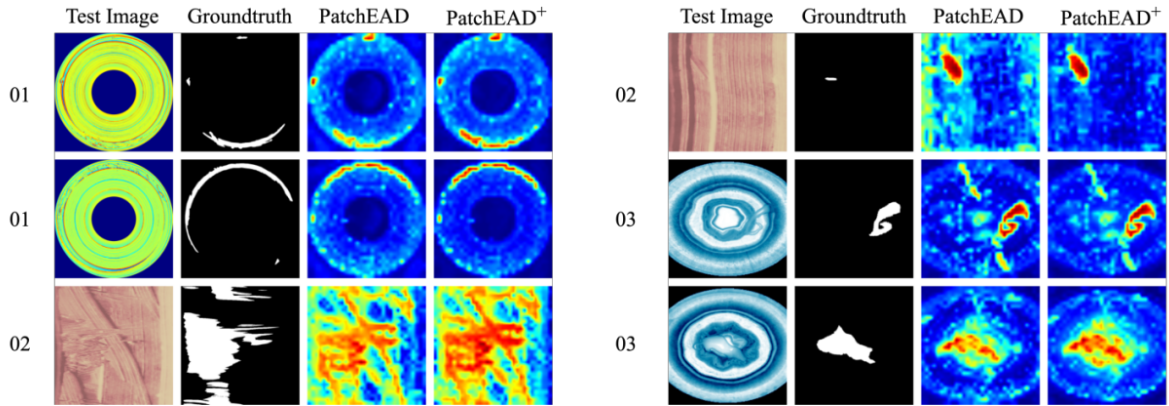


Figure 13. Additional visualization results from PatchEAD and PatchEAD+(0-shot), tested on BTAD.

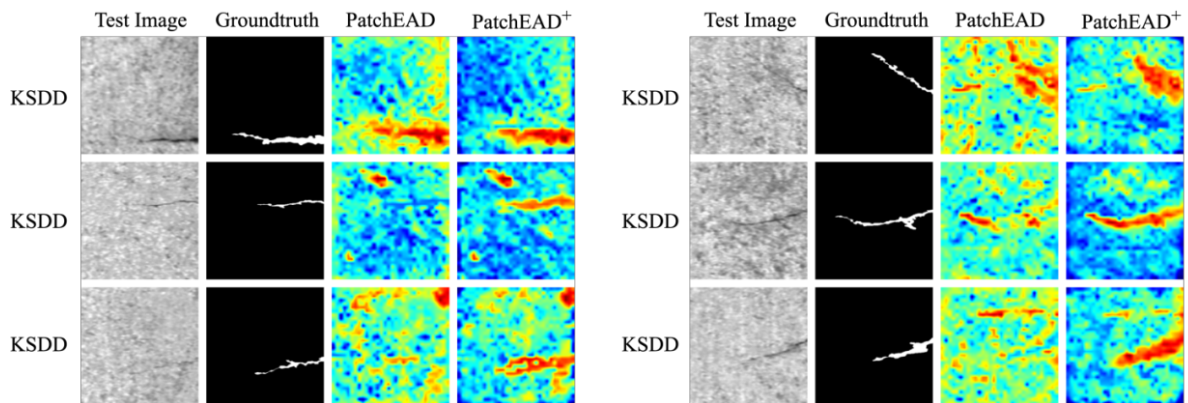


Figure 14. Additional visualization results from PatchEAD and PatchEAD+(0-shot), tested on KSDD.

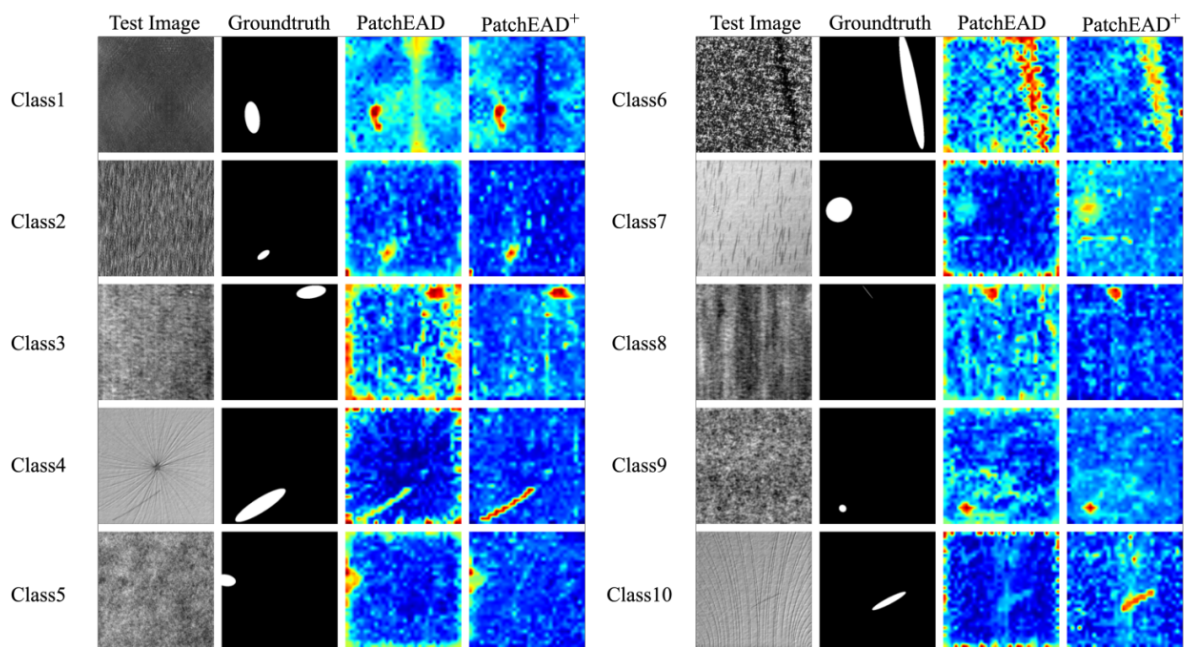


Figure 15. Additional visualization results from PatchEAD and PatchEAD+(0-shot), tested on DAGM.

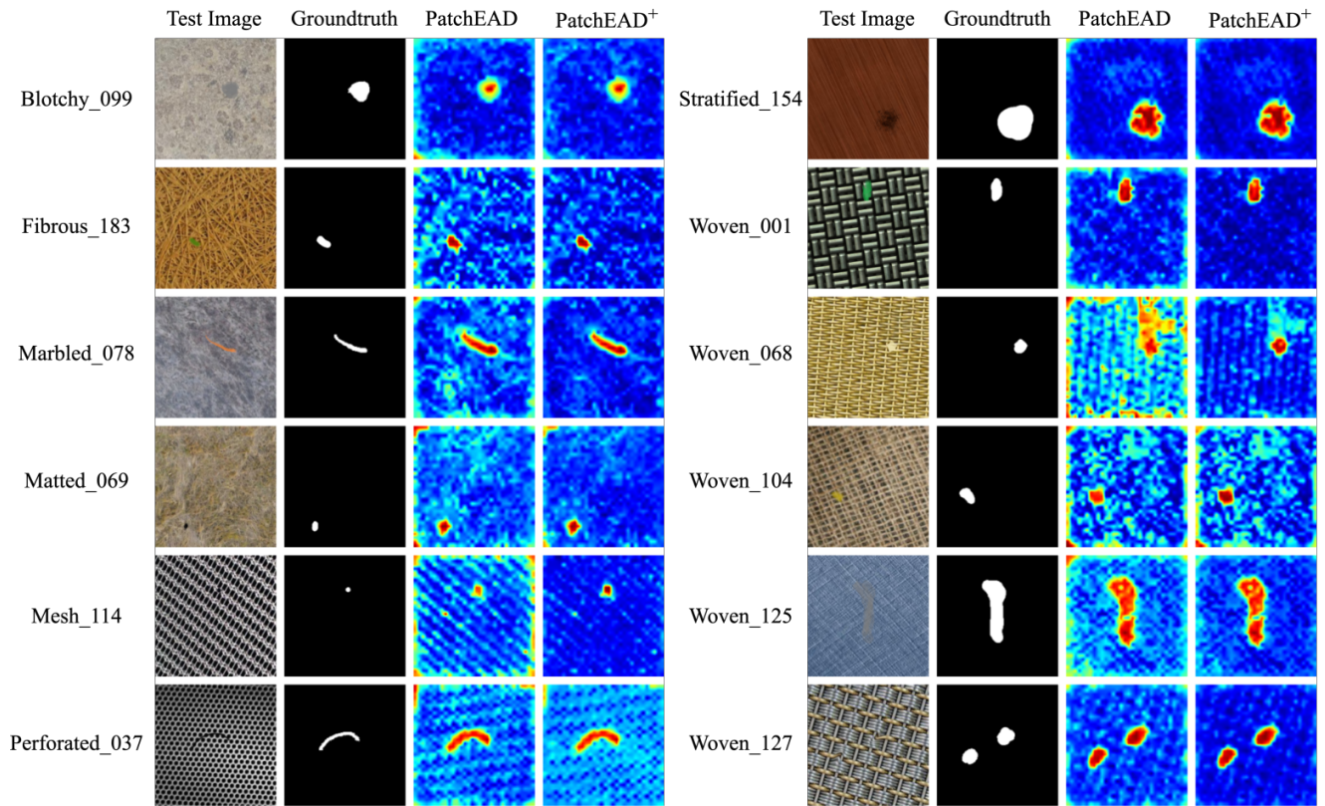


Figure 16. Additional visualization results from PatchEAD and PatchEAD+(0-shot), tested on DTD-Synthetic.

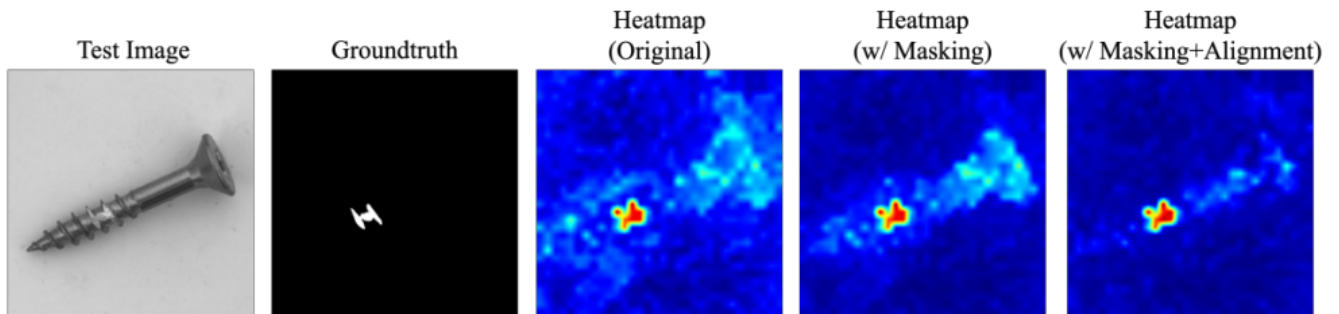


Figure 17. Additional visualization results for the comparison to evaluate the effectiveness of Alignment and Masking.